UNIVERSITY OF CALIFORNIA,
IRVINE

Fabrication of Copper Inverse Opals for Microscale Liquid Transport in Polycrystalline Porous Media

DISSERTATION

submitted in partial satisfaction of the requirements
for the degree of

MASTER OF SCIENCE

in Mechanical and Aerospace Engineering

by

Quang Nhat Pham

Dissertation Committee:
Assistant Professor Yoonjin Won, Chair
Associate Professor Lorenzo Valdevit
Associate Professor Ali Mohraz

2018

DEDICATION

To my family, around the world.

TABLE OF CONTENTS

LIST OF FIGURES

ACKNOWLEDGMENTS

I am grateful to my advisor, Yoonjin Won, for giving me the opportunity to conduct research, supporting my projects, and continuing to believe in me. Special thanks to Michael Barako, whose guidances and mentorship were invaluable to the development of my projects. I am always thankful to have my family as the foundation within my life and being only a phone call away.

Thank you Krista for being my best friend who taught me patience and kindness, Laia for making everyday an enjoyable experience in lab, and all my labmates and friends who helped me grow as a scientist.

CURRICULUM VITAE

Quang Nhat Pham

EDUCATION

Master of Science in Mechanical Engineering **2018**
University of California, Irvine *Irvine, California*

Bachelor of Science in Mechanical Engineering **2015**
University of Virginia *Charlottesville, Virginia*

Bachelor of Arts in Studio Art (Painting) **2015**
University of Virginia *Charlottesville, Virginia*

RESEARCH EXPERIENCE

Graduate Research Assistant **2015–2018**
University of California, Irvine *Irvine, California*

Undergraduate Research Assistant **2012–2015**
University of Virginia *Charlottesville, Virginia*

Research Assistant Intern **2014–2014**
Commonwealth Center for Advanced Manufacturing *Disputanta, Virginia*

Research Consultant Intern **2014–2014**
Volkswagen AG *Wolfsburg, Germany*

TEACHING EXPERIENCE

Teaching Assistant **2016–2016**
University of California, Irvine *Irvine, California*

JOURNAL PUBLICATIONS

Hierachical and Well-Ordered Porous Copper for Liquid Transport Properties Control **2018**

Pham, Q.N., Shao, B., Kim, Y. and Won, Y. *ACS Applied Materials & Interfaces*. 10, 16015.

Controlled Wetting Properties through Heterogeneous Surfaces Containing Two-level Nanofeatures **2017**

Dubey, P.P., Pham, Q.N., Cho, H., Kim, Y. and Won, Y. *ACS Omega*. 2, 7916.

Microscale Liquid Transport in Polycrystalline Inverse Opals across Grain Boundaries **2017**

Pham, Q.N., Barako, M.T., Tice, J. and Won, Y. *Scientific Reports*. 7, 10465.

Effect of Growth Temperature on the Synthesis of Carbon Nanotube Arrays and Amorphous Carbon for Thermal Applications **2017**

Pham, Q.N., Larkin, L.S., Lisboa, C.C., Saltonstall, C.B., Qiu, L., Schuler, J.D., Rupert, T.J. and Norris, P.M. *Physica Status Solidi A*. 214, 1600852.

Thermal Conductivity of Vertically Aligned Carbon Nanotube Arrays: Growth Conditions and Tube Inhomogeneity **2014**

Bauer, M.L., Pham, Q.N., Saltonstall, C.B. and Norris, P.M. *Applied Physics Letter*. 105, 151909.

CONFERENCE PRESENTATIONS

Boiling Heat Transfer Performance of Three-Dimensionally Ordered Microporous Copper with Modulated Pore Diameters **June 2018**

Intersociety Conference on Thermal and Thermomechanical Phenomena in Electronic Systems (ITherm), San Diego, CA, USA

Spatially Arranged Copper Inverse Opal Architecture for Highly-Ordered Flow Field in Boiling. **March 2018**

International Conference on Boiling and Condensation Heat Transfer, Nagasaki, Japan

Extreme Microfluidic Evaporative Cooling through Gradient Crystalline Porous Structures. **Nov 2017**
International Mechanical Engineering Congress and Exposition (IMECE), Tampa Bay, FL, USA

Electrochemically Etched Copper Inverse Opals: Permeability and Wettability Control **July 2017**
DROPLET Conference, Los Angeles, CA, USA

Copper Inverse Opal Architectures for Evaporative Cooling Applications **Jan 2017**
Micro and Nanoscale Phase Change Heat Transfer Gordon Research Conference , Galveston, TX, USA

Gradient Copper Inverse Opal Structures for Phase Change Heat Transfer **June 2016**
ASME 2016 Summer Heat Transfer Conference, Washington, D.C., USA

Nanoflower and Nanograss Features on Inverse Opal Structures **Apr 2016**
Southern California Society for Microscopy and Microanalysis, Irvine, CA, USA

Fabrication of Copper Inverse Opals on Conformal Microscale Patterns **Mar 2016**
2016 International Conference on Micromanufacturing (ICOMM), Irvine, CA, USA

Synthesizing High Purity Single-walled Carbon Nanotube Arrays for Thermal Applications **Nov 2013**
ASME 2013 International Mechanical Engineering Congress and Exposition (IMECE), San Diego, CA, USA

HONORS AND AWARDS

Best Paper Award, Intersociety Conference on Thermal and Thermomechanical Phenomena in Electronic Systems (2018)

Poster Award, Southern California Society for Microscopy and Microanalysis Conference (2016)

Academic Dean's List, University of Virginia (2014)

Rodman Scholar, University of Virginia (2011)

ABSTRACT OF THE DISSERTATION

Fabrication of Copper Inverse Opals for Microscale Liquid Transport in Polycrystalline Porous Media

By

Quang Nhat Pham

Master of Science in Mechanical and Aerospace Engineering

University of California, Irvine, 2018

Assistant Professor Yoonjin Won, Chair

The continually increasing power density of high-performance electronics is bottlenecked by the challenges faced with thermal management requirements for reliable operation. While the traditional convective air-cooling approach is limited in its effectiveness at dissipating high heat fluxes, the use of latent heat in liquid-vapor phase change is an attractive strategy for managing the most aggressive thermal loading demands. Passive two-phase cooling operates by capillary pumping fluid through void spaces within porous metals to transport energy over long distances. The performance of such liquid delivery through porous structures is governed by the pore distribution, porosity, and morphology. Analogous to energy transport in polycrystalline solids, hydraulic transport in polycrystalline porous media is also limited by structural defects and grain boundaries. This work reports on the capillary performances of both single- and polycrystalline microporous copper with varying pore diameters from 300 to 1000 nm. The hydraulic transport through the arrays of interconnected spherical pores is modeled and quantified with experimental wicking measurements, and the influence of grain boundaries on the hydraulic transport in polycrystalline microporous media contributes to the hydraulic resistance presented by the structural defects. By combining multiple pore diameters and systematically layering them, this study creates heterogeneous porous media to emulate the transport within biological systems. The gradient layering

of pores enhances the liquid delivery by circumventing grain boundary defects in three dimensions. The fundamental understanding of hydraulic transport physics through porous crystals and boundaries will pave the way for the spatial design of heterogeneous porous materials for future capillary-driven technologies.

Chapter 1

Introduction

With increasing power densities in microprocessors [1], radar amplifiers [2], and laser diodes [3], the ability to effectively manage the thermal conditions of electronic components becomes a daunting challenge [4, 5]. Massive heat flux dissipation is often bottlenecked by the physical limitation associated with thermal management strategies. Traditional finned heat sinks are often used in conjunction with a fan or other means of convective cooling. However, such method of thermal conduction and forced air convection possess limited heat removal capacity. As power-dense electronics exceed the thermal dissipation capability of traditional finned heat sinks, new and advanced thermal solutions with higher heat transfer performance are needed.

A promising alternative that has garnered increasing interest is the use of phase-change heat transfer devices such as thermal ground planes, vapor chambers, and heat pipes (see Figure 1.1 for schematic diagram), which presents an order of magnitude enhancement in heat transfer coefficient than traditional forced air convection [6]. The enhancement of two-phase heat transfer is, in part, due to their effective usage of the latent heat of vaporization. Another major advantage in planar type devices is the lack of external pumping required for

fluid transport. The self-sustaining pumping mechanism of the working fluid is performed by the passive capillary force created by the microporous wicking structure.

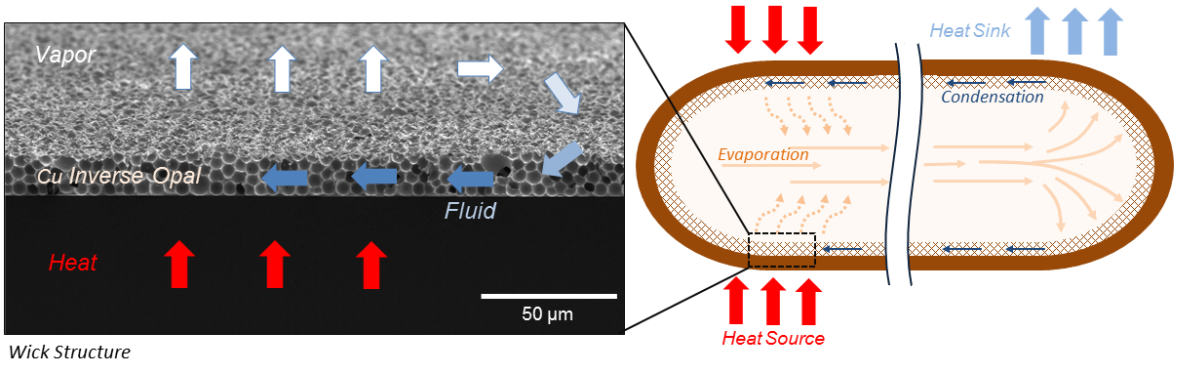

Figure 1.1: Schematic diagram of a heat pipe.Thermal dissipation occurs by evaporating the working fluid and transporting it over a distance to be cooled. The condensed liquid then returns to heat source by means of capillary forces induced by the porous wicking medium.

1.1 Background

Traditional porous media used in two-phase heat transfer applications have included channels, grooves [7], meshes [8], which have features in the range of millimeters and microns. While such fairly large feature sizes are easy to manufacture, they possess limited capillary pressure that require additional pumping mechanisms to drive the flow of fluid. This contributes to the complexity and bulkiness in device designs. Others novel micro- and nanoscale porous media such as sintered powder [9, 6, 10], carbon nanotube arrays [11] serve as promising alternatives to traditional porous media through their enhanced capillary-driven transport capability. The low dimensions of such porous structures also make them ideal for compact microelectronic applications. However, the nonuniformity and amorphous structural arrangement of these microporous media makes the modeling of their hydraulic transport difficult and unpredictable. While their effective transport physics can be ascertained, a "unit cell" of an amorphous media with random and tortuous pathways are often difficult to reproduce and study at the microscale level. Other capillary-fed wicking media includes sil-

icon micropillars [12, 13], which possess well-ordered periodic structural features. However, traditional microfabrication process exhibit limitation in structural material choices (i.e., silicon and complementary metal oxide semiconductor) and modulation of three-dimensional features [14].

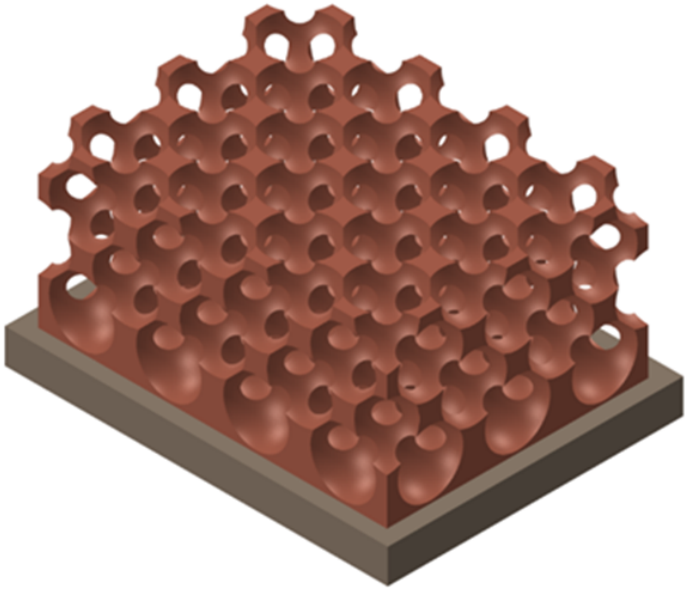

Figure 1.2: A model of inverse opal as a three-dimensionally ordered porous media with interconnected spherical pores.

Recent advances in template-assisted micro- and nanofabrication technique provides opportunity to create novel architectures of crystalline and semi-crystalline porous media. A relatively new class of crystalline porous media that yields uniform, periodic, and continuous arrangement of spherical pores is known as inverse opals (IOs) [15, 16, 17, 18]. The well-ordered arrangement of IOs (see Figure 1.2) attracts a wide range of applications, which includes photonic crystals [19, 20], electrodes [21, 22, 23], and microfluidic heat exchanger [24, 25]. Within the inverted close-packing structure, each spherical pore is connected to adjacent pores by a circular interconnected window (called the "via") formed from the templated sphere-to-sphere contact points to create a continuous fluid-permeable pathway through the entire IO (i.e., open-cell morphology). The large surface area-to-volume ratio and high permeability of metallic IOs promises enhanced energy transport through a solid and energy

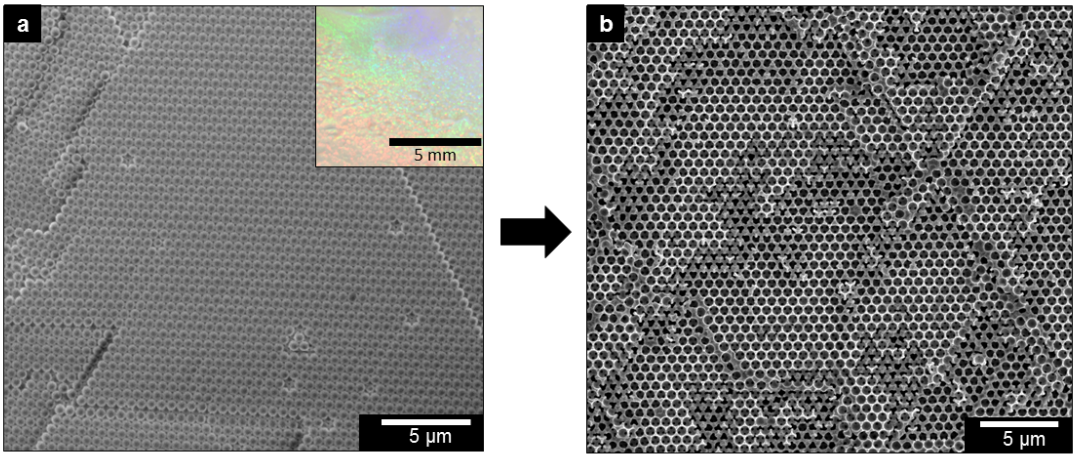

Figure 1.3: The crystalline arrangement of a) self-assembled opal and b) inverse opal. The inset in a) demonstrates the overall crystallinity of the opal film through optical light diffraction.

exchange across a large solid-fluid interfacial surface area. The structural arrangement of IOs is an inverted replica of the original opal template. For instance, by self-assembling the opal film into crystalline formation, the resulting IO will possess a highly-ordered pore matrix, as shown in Figure 1.3. The ability to modulate the polymeric template design allows for a systematic investigation of structure-property correlations between pore morphologies (i.e., porosity, pore diameters, and structural arrangement) and liquid delivery performances.

Despite possessing highly-ordered packing of spheres at small length scale (10 μm), the colloidal crystal forms propagated cracks [26] at larger length scale caused by opal film drying, as shown in Figure 1.4a. The inversion of these cracks results in "grain boundary" formation between crystalline IO domains (see Figure 1.4b). The polycrystalline nature of semi-ordered material plays a significant role in the transport kinetics across crystalline defects and therefore should be fully understood. Much like energy transport in polycrystalline solids, hydraulic transport in semi-ordered porous media is limited by the hydraulic resistance presented by grain boundaries between pore domains. Computational modeling of fluidic transport through regular unit cells consisting of close-packing pores can predict the upper and lower limits of transport properties in crystalline IOs, and the empirical deviations

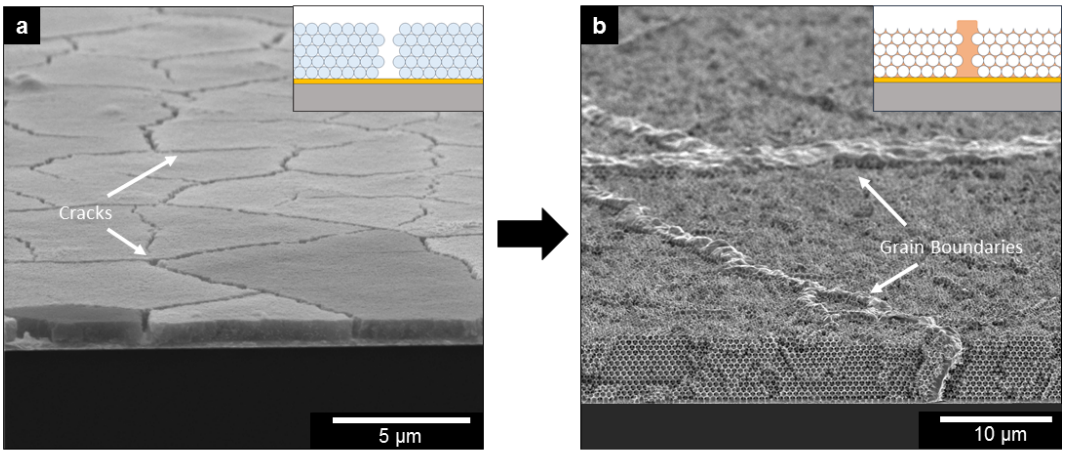

Figure 1.4: The polycrystalline nature of the a) opal template causes the b) inverse opal to form grain boundaries that separate crystalline pore domains.

from such predictions can be mainly contributed to the hydraulic resistance associated with grain boundaries in polycrystalline IOs. The quantified values in transport performance in single- and polycrystalline IOs will elucidate fundamental insights toward understanding, predicting, and engineering microfluidic transport through monoporous crystalline IOs.

Chapter 2

Copper Inverse Opals

2.1 Introduction

Inverse opals (IOs) structures have garnered intense interest due to its three-dimensional well-ordered porous arrays, large surface area, short diffusion lengths [27], and increased active site accessibility for enhanced mass transport [28], reaction activity [29, 30], and sensing capability [31]. While IO architectures have been thoroughly examined for uses as photonic crystals [20, 32] , catalysis [33, 34], and power storage [35, 36], only limited reviews have explored IOs as an ideal wicking material in electronics cooling systems [24, 25].

Sintered powder have been traditionally used as the wicking medium in liquid-vapor cooling devices [37, 38, 39, 40] due to its rapid throughput, facile production, and economically viable. However, the periodic and highly interconnected microporous architecture of IOs possesses several advantages in convective cooling applications. While sintered powder has reported porosity ranging from 30 to 45% [6, 9], IOs have approximately twice the structural porosity [26, 41], increasing both the effective surface area and permeability for enhanced heat transfer rate. The pore sizes in sintered powder can also vary drastically due to the polydisperse

particles [6] in comparison to the homogeneous distribution of IO pore sizes as derived from colloidal monodispersity. Lastly, the templating process can be used to engineer novel nanomaterials by accommodating both intricate geometries and desirable material selection, which decouples the typical constraints posed by traditional nanofabrication. For instance, depositing desired materials such as silica [42], titania [43, 42, 44, 45] , or polymer [46, 47] can produces IOs with various structural framework. In the applications of microfluidic heat exchanger, metallic IOs [18, 25] may prove to be optimal due to the higher material thermal conductivity. Therefore, copper is of significant interest and is used as the IO structural material in this study.

By controlling the layout of the sacrificial opal template through selective pore arrangement and pore diameters, various architectural design of IOs can possess unique singular characteristic or combinations of structural features. For instance, by layering stratus of different pore diameters on top of each other, heterogeneous porous media can be constructed. In this work, both monoporous (i.e., uniform pore size and spatial distribution) and gradient (i.e., spatially-varying pore size) copper IOs are fabricated to examine their transport phenomena.

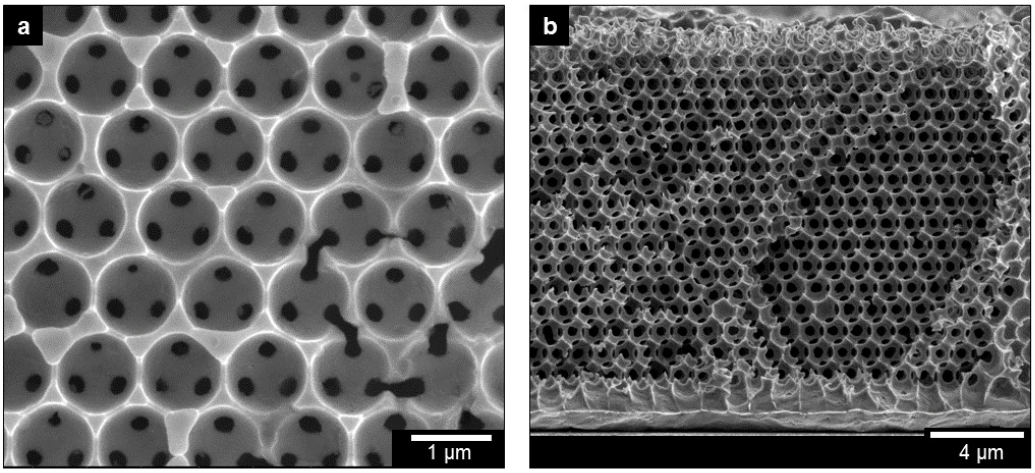

Figure 2.1: SEM of monoporous copper inverse opal as shown from a) plan and b) cross-sectional view.

2.1.1 Monoporous Inverse Opal Architecture

Monoporous copper IOs are characterized by crystalline packing of uniform-sized pores (a representative IO is shown in Figure 2.1). The homogeneous pore diameter derived from the monodisperity of the polystyrene spheres forms the sacrificial opal template. Homogeneous porous arrays permit predictable and repeatable modeling of fluid transport through the IOs.

2.1.2 Gradient Inverse Opal Architecture

Despite the attractiveness of uniform and homogeneous structures in permeable media, fluid and mass transport in nature often occurs through complex heterogeneous porous material with multiple length scale pores. For instance, plants and animals have evolved to efficiently transfer nutrients, gases, and macromolecules within porous networks with regularly decreasing pore sizes, as demonstrated with leaf veins, mammalian vascular and respiratory systems [48, 49, 50]. While the understanding of liquid delivery for monoporous media is fundamental to transport principles, the spatial design of three-dimensional heterogeneous porous structure found in nature motivate the desire to create gradient IOs (i.e., spatially varying pore sizes normal to the substrate). Although several studies demonstrated the fabrication of rationally-designed heterogeneous porous crystals, these methods utilized a variety of complex techniques. For instance, Huang *et al.* used plasma etching to incrementally reduce the IO size for each layer [45], and Yan *et al.* stacked different opal size films on top of each other by transfer method [44]. The fabrication processes require multiple steps and delicate control of the opal film. The presented work successfully demonstrates gradient copper IOs (see Figure 2.2) by using a simple and reliable layer-by-layer growth through repeated convective vertical deposition to stack multiple layers of different sphere sizes [42, 43].

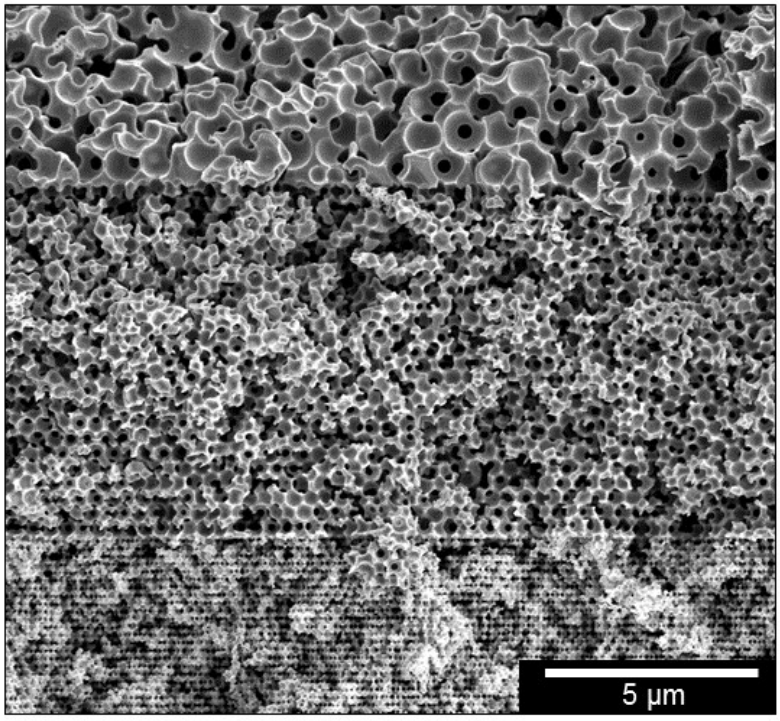

Figure 2.2: Cross-sectional SEM of gradient copper inverse opal with three strata of different pore sizes normal to substrate.

2.2 Fabrication

Monoporous and gradient copper IOs are fabricated using self-assembly vertical deposition [42, 43] and electrochemical deposition [18], which is shown to be a simple, inexpensive, and reliable method in creating crystalline IOs (Figure 2.3). First, electron-beam evaporation deposits 20 nm thick titanium and 80 nm thick gold onto a silicon wafer through shadow masks (7 mm x 5 mm in size), which is used as the working substrate. A self-assembled monolayer (SAM) forms on the gold surface after immersion in a 1 mM aqueous solution of sodium 3-mercapto propanesulfonate (3-MPS) for 24 hours. The negatively charged tail of the SAM makes the gold surface highly wettable, which is essential for the self-assembly vertical deposition process. The substrates are then rinsed with deionized (DI) water and vertically immersed in a well of colloidal suspension, as illustrated in Figure 2.3a. The colloidal suspension composes of monodispersed polystyrene spheres (Thermo-Fisher) diluted in

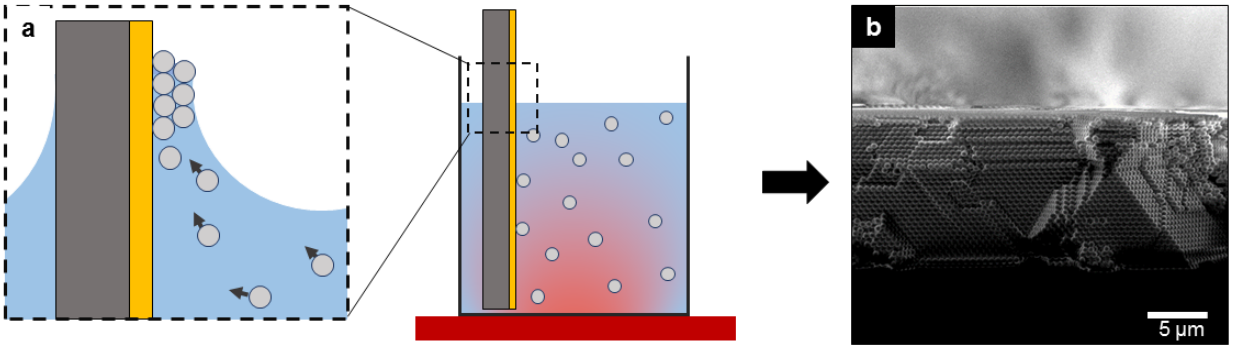

Figure 2.3: a) Schematic of template-assisted vertical deposition process. Colloids self-assemble onto the hydrophilic gold coated substrate at the triple contact line. A heated base gently mixes the colloids and prevents sedimentation. As the suspension evaporates, b) crystalline opal film forms as confirmed with cross-sectional SEM.

DI water to possess mass concentration of 0.6 %w/v. The polystyrene spheres with diameters 300, 600, and 1000 nm are chosen. By placing a hot plate underneath the well, the solvent evaporates at a controlled temperature of 55 ± 1 °C, as confirmed with a thermocouple at the base of the well. The base heating of the well induces a gentle convective mixing of the colloids to prevent sedimentation. As the solvent evaporates, the capillary force at the triple contact line pulls the sphere particles toward the hydrophilic substrate to self-assemble into crystalline opals (see Figure 2.3b). The number of deposited opal layer is strongly governed by the changes in colloidal concentration, which can be used to tune the thickness of the opal film (more details provided in Chapter 2.3.1). The crystallinity of the opal can be optically observed from light diffraction and corroborated with top and cross-sectional SEM images, as previously shown in Figure 1.3.

The fabrication process of gradient IOs is similar to that of monoporous IOs. However, after the deposited opal film dries, it is then reimmersed in a suspension of another arbitrary sphere size. This subsequent colloidal deposition is used to stack layers of different sphere diameters and can be repeated to fabricate the desired gradient opal structure (see Figure 2.5 for preparation outline). While there can be numerous variations of gradient IO designs, the combination of sphere diameters used for stacking as well as the stacking order of spheres

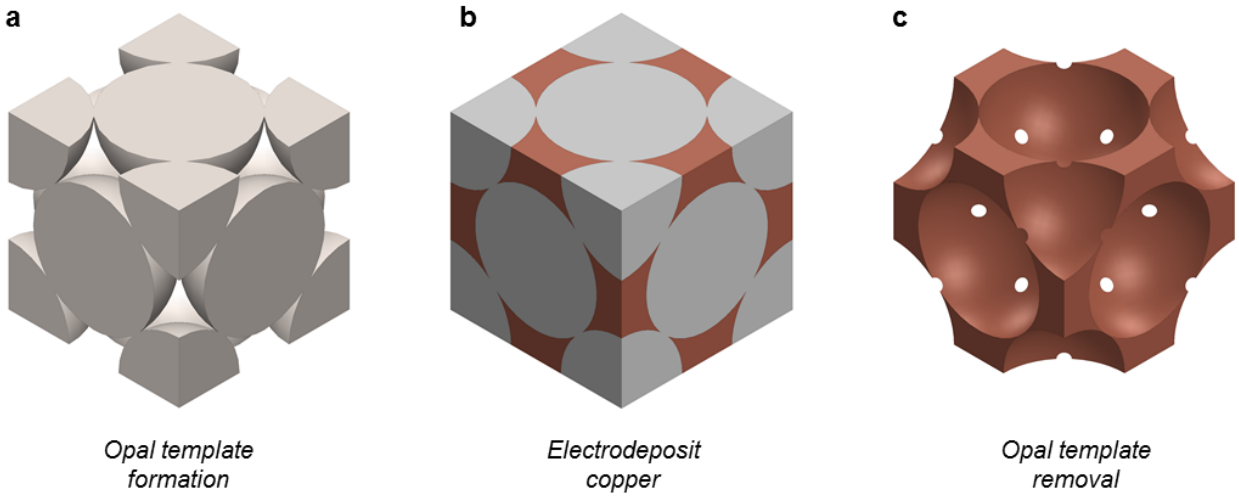

Figure 2.4: Unit cell schematic for the preparation of inverse opals. a) After the colloids self-assemble into crystalline opal, b) copper is then electrodeposited into the cavities between the colloids. c) The removal of the sacrificial colloids reveals a copper inverse opal structure.

can be limited (see Chapter 2.3.3 for more details.).

Afterward, the opal template of both monoporous and gradient structure anneals in a furnace oven for 5 hours at 97 ± 1 °C, monitored by a thermocouple attached to supporting copper base plate to induce uniform sintering of the samples. The annealing process causes the sacrificial polystyrene spheres to coalesce, increasing the sphere-to-sphere contact area for improved thin film structural stability and increase porosity, which is further explained in Chapter 2.3.2. Copper then electrodeposits into the voids between spheres using galvanostatic mode (BioLogic, USA) in a three-electrode cell at room temperature. In this set-up, a copper plate and a saturated Ag/AgCl is used the counter electrode and reference electrode, respectively. The distance between the counter and working electrode remains fixed at 2.5 cm. The electrodeposition is conducted in an electrolyte composed of 0.5 M $CuSO_4$ and 0.1 M H_2SO_4 at a constant current of -1.875 mA versus the reference electrode (or 0.53 mA/cm^2 in current density). The thickness of the deposited copper correlates to the electrodeposition time, which can be controlled to obtain the desired number of IO layers (see Chapter

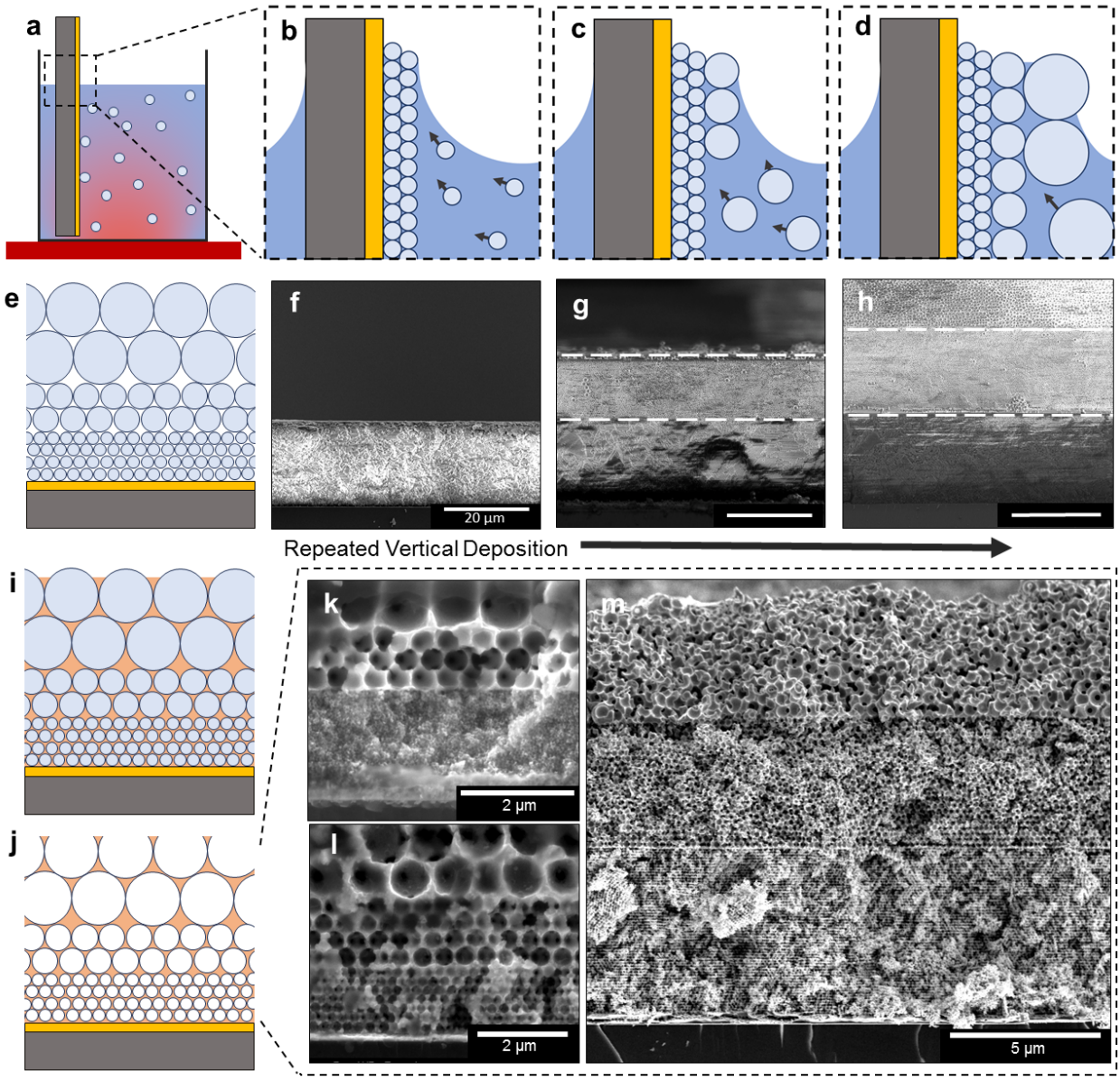

Figure 2.5: The fabrication process for creating gradient copper inverse opals. a-b) Colloids self-assemble onto the gold substrate during vertical deposition and c-d) subsequent repeated trials can stack different sphere diameters. An example with stacked spheres are shown as a diagram in e) and SEM images in f-h). After i) electroplated copper infiltrates the cavities between the spheres, j) the sacrificial spheres are removed to reveal inverse opals with various combinations of gradient spatial arrangement, as shown with SEM images in k-m).

2.3.1 for more details). Afterward, the templated polystyrene spheres dissolve in a bath of tetrahydrofuran for at least 1 hour. The chemical etchant traverses throughout the porous structure to dissolve polystyrene spheres through the interconnected via between the pores. The sample is then rinsed with DI water and dried with compressed air.

2.3 Fabrication Parameters

Since the final IO architecture is dictated by the opal template, the majority of the IO design opportunities derive from within the self-assembly stage. Understanding the effects of fabrication parameters on the structural characteristics of the self-assembled opals as well as the IOs (i.e., media thickness, porosity, pore arrangement, and defects formation) will provide insights toward selective tuning of transport mechanics. The set of parameters detailed in the preparation of IO (Chapter 2.2) for transport study is selected after thorough investigation and analysis. In the following subsections, several of these parameters will be highlighted by systemically studying and rationally designing copper IOs with controllable morphological characteristics.

2.3.1 Opal and Inverse Opal Thickness

The number of deposited opal layers is dependent on the colloidal concentration [51], sphere size [52, 46, 53] , and base heating temperature [54, 53] during the self-assembly vertical deposition process. As shown in Figure 2.7, the changes in colloidal concentration of smaller sized spheres affects significantly more on the deposition layer thickness than larger sized spheres. This may be because at the same mass concentration, there are higher counts of smaller spheres present in comparison to larger, heavier spheres. The smaller spheres are also less prone to sedimentation, and the gentle convective mixing helps to resupply the

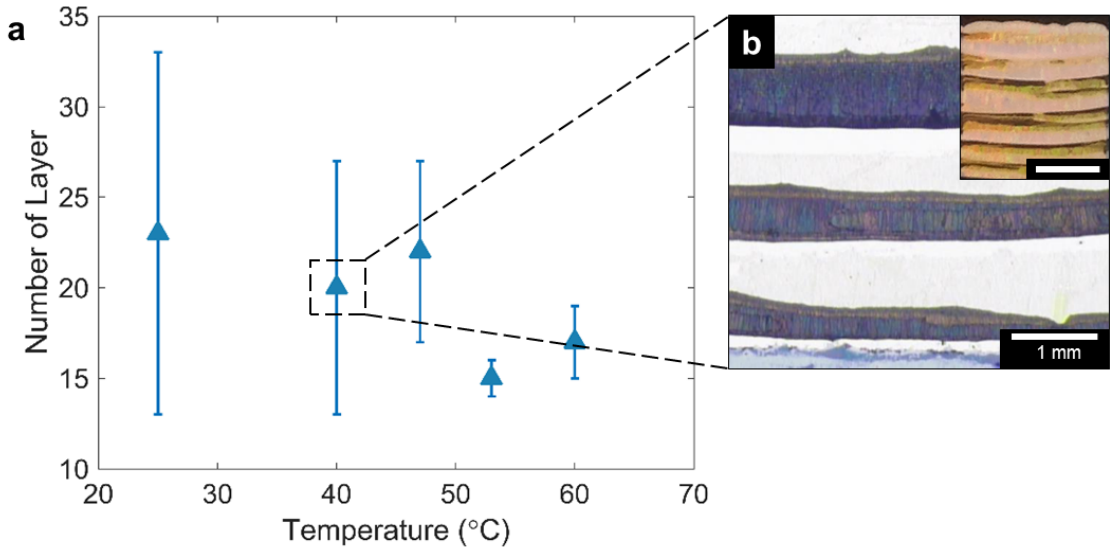

Figure 2.6: a) Deposition thickness of opal film as a function of base heating temperature. Base heating is needed to ensure uniform self-assembly of sacrificial spheres. Approximately 55 °C is shown to be the optimum temperature in yielding the most consistent and crystalline opal formation. Lower temperatures causes nonuniform opal deposition as shown with top view optical microscope and camera capture from b) and inset, respectively. The opal thickness measurement is based on the corresponding 60 nm diameter polystyrene spheres at 0.04 %w/v concentration. Scale bar of inset is 2 mm.

meniscus-substrate-contact region with a sufficient supply of colloidal particles for larger number of deposited layers. The induced convective mixing is controlled by the base heating during vertical deposition. Various process temperatures are analyzed to control evaporation rate and opal film thickness (Figure 2.6a). Based on the results, an optimal process temperature of ∼55 °C produces the most uniform opal film thickness and is used for the remaining of the experiments. The significant variances in opal film thickness at lower heating temperature arise from the fluctuations between sphere sedimentation and deposition, which fail to consistently resupply the spheres toward the evaporative meniscus front. The lack of spheres causes the meniscus to slip along the drying direction, which forms periodic stripes of coalesce opals as well as regions with no spheres (see Figure 2.6b) for representative microscopic and top-view camera capture). Similar nonuniform deposition patterns are also observed with excessively diluted suspension such that insufficient amount of spheres are available to self-assemble into arrays.

By considering the evaporation rate to be equal to the colloidal film growth rate during vertical deposition, we can predict the thickness of as-produced multilayer opals according to [52, 46]:

er

$$n = \frac{\beta L \phi}{0.605 d(1-\phi)} \tag{2.1}$$

where n is the number of layer, L is the meniscus height, β is the ratio between the velocity of a particle in the solution and velocity of the fluid, and is taken to be unity for dilute suspensions of weakly interacting particles [46], d is the particle diameter, and ϕ is the particle volume fraction in the solution. The thickness measurements presented in Figure 2.7 shows good agreement with the model from Equation (2.1) (dashed line), where the parameters are given by the sphere size and colloidal concentration and the fitting parameter is the meniscus height L. In addition, the equation also validates our theory that evaporation rate, as controlled by the base heat temperature, is not a major factor in determining opal deposition thickness.

While the opal film thickness is determined by vertical deposition parameters, the IO thickness is dependent upon the electrodeposition process. Using galvanostatic mode, the level of electrodeposited metal filling the cavities of the colloidal crystal template (i.e., IO thickness) can be controlled using the *in situ* potential transient measurement [18, 55, 56]. A typical galvanostatic measurement during copper electrodeposition into the voids between opal template is shown in Figure 2.8, which exhibits a voltage damping oscillation behavior [57]. The oscillations represent the varying electrochemically available surface area as copper fills up around the curvature of the packed spheres along each opal layer [55]. That is, the smallest available surface area (i.e., the valleys in the oscillations) corresponds to the center of the spheres of that associated layer and each peak corresponds to the completion of a

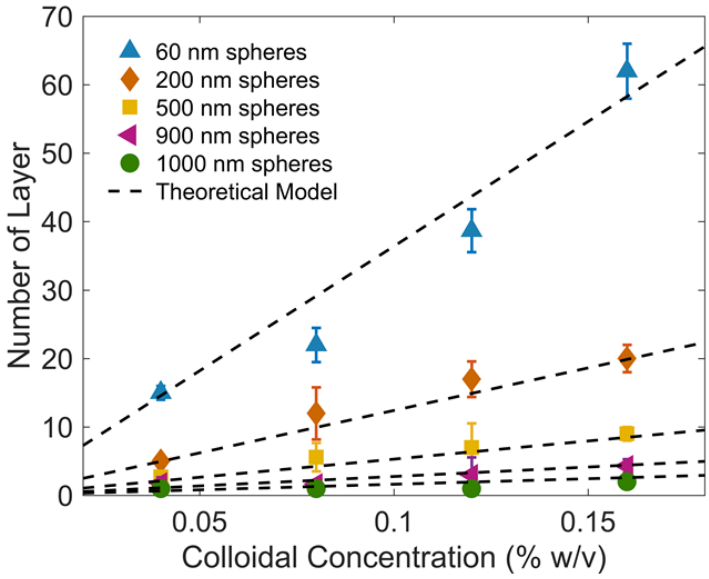

Figure 2.7: Variation of colloidal concentration on the number of deposited opal layers for different monodispersed sphere sizes with a base heating temperature of 55 °C. The dashed line indicates expected thickness (Equation 2.1).

single IO layer. The continually decreasing damping oscillations is a result from increasingly anisotropic galvanostatic copper growth with each opal layer due to uncontrollable metal deposition and template defects such as vacancies, stacking faults, and cracks. The existence of voltage oscillations during electrodeposition suggests that the majority of the opal template is crystalline and that metal growth is fairly uniform.

2.3.2 Annealing

After the self-assembly of opal film, the spheres are annealed to increase the contact areas between adjacent spheres [58, 41], called the neck. After copper electrodeposits into the empty volume between spheres, the spheres are dissolved to create an inverted structure, such that the necks become interconnected windows between adjacent pores, denoted as the via. The open cell-arrangement creates a continuous, fluid-permeable network of pores. Thus, the annealing process serves two functions: 1) enhances the structural integrity of the opal film

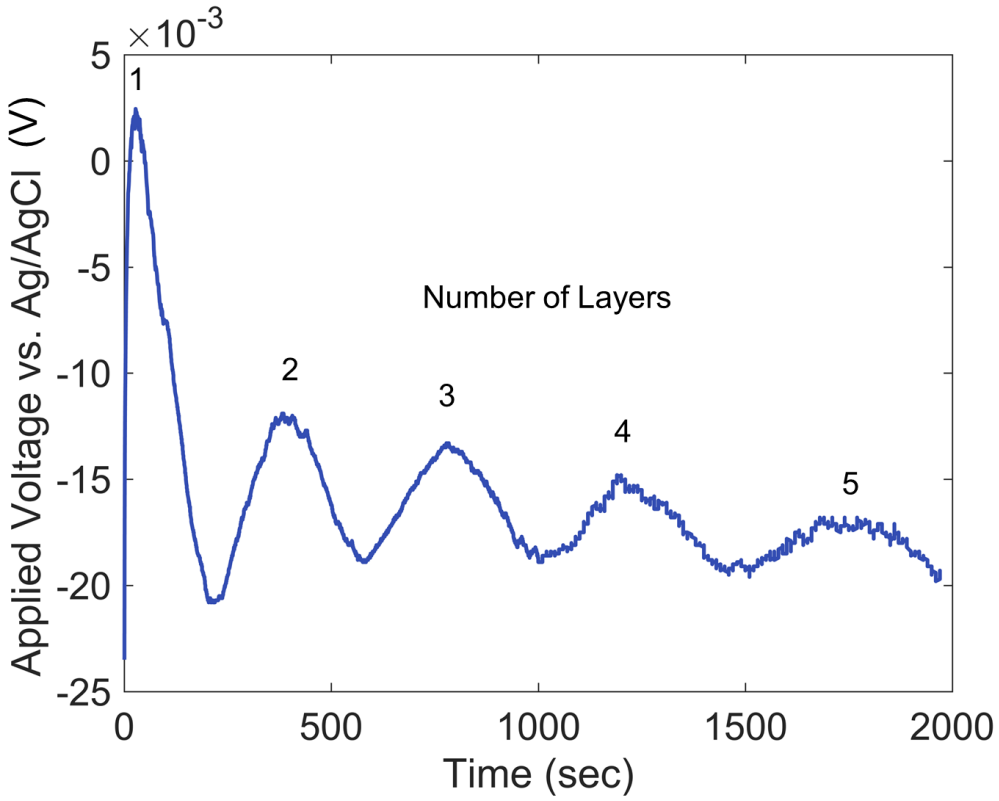

Figure 2.8: A typical galvanostatic electrodeposition characteristic of electrodeposited copper into the voids of a colloidal crystal. The current remains constant at -1.875 mA over a total seed gold layer area of 30 mm^2.

and 2) increases the porosity of the IO structure by opening up the via [59]. By modulating the annealing temperature and time, the via diameter D_{via} can be tuned to determine its structural porosity ϕ through a derived numerical correlation using computational fluid dynamics (CFD) which is valid for $78\% < \phi < 92\%$:

$$\phi = \frac{0.58 D_{via}}{D_{pore}} + 0.66 \tag{2.2}$$

where D_{pore} is the pore diameter as controlled by the templated sphere size. More information regarding this computational fluid dynamics calculations can be found in Chapter 2.4. The normalized ratio of via diameters to pore diameters D_{via}/D_{pore} is measured through post-

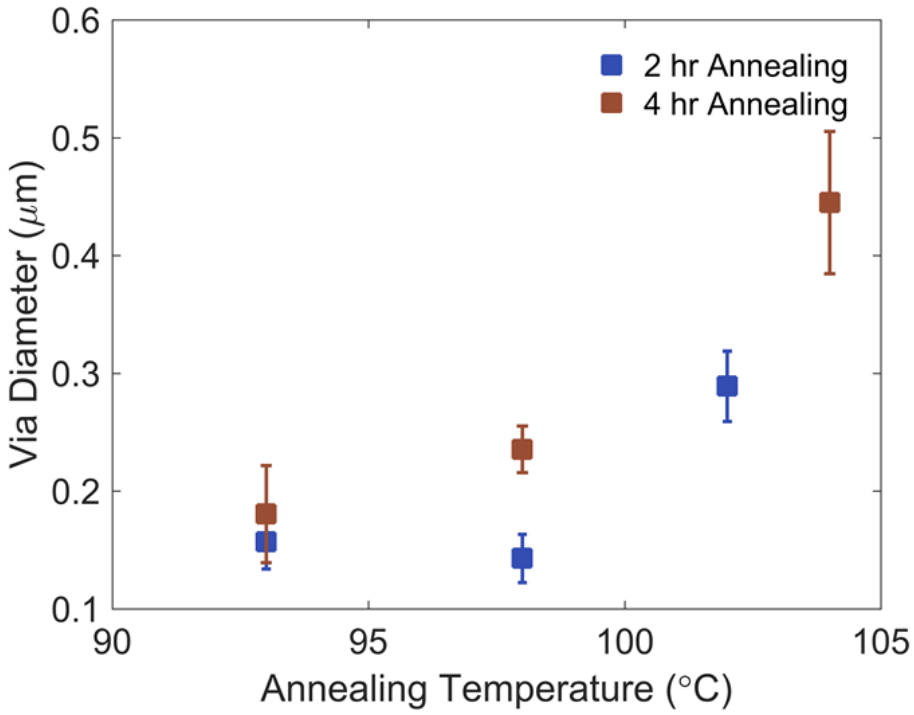

Figure 2.9: The effect of annealing temperature and time on via diameter. Increasing the extent and degree of annealing causes spheres to coalesce more, resulting in inverse opals with larger via diameters.

image processing. The correlation is based on the assumption that the sintering of spheres occurs isotropically, spheres self-assemble into close-packed crystalline arrangement, and spheres remain perfectly round.

The annealing results with temperature range of 93 °C to 104 °C on the D_{via} of 1000 nm sphere diameter are shown in Figure 2.9. The furnace temperature is confirmed with a thermocouple attached to the supporting copper plate that holds the opal samples for uniform heating. While the sintering time does affect the via diameter D_{via}, the annealing temperature is more effective in modulating the D_{via}. The selected furnace temperatures are well below the glass transition temperature of polystyrene [60]. However, as the sintering process approaches the glass transition temperature, the crystallinity of the IOs degrades due to the significant enlargement of D_{via} such that pores and via become unrecognizable

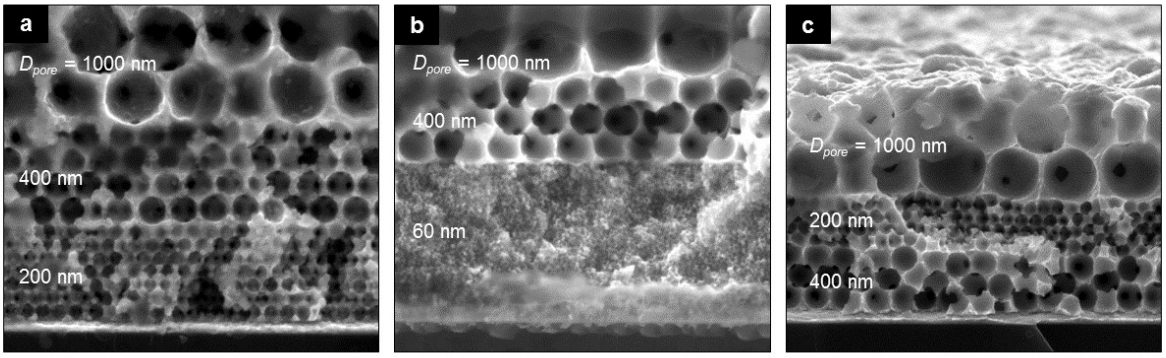

Figure 2.10: Cross-sectional SEM images showing various combinations of gradient copper inverse opals with stacks of a) 60, 400, and 1000 nm pore diameter; b) 200, 400, and 1000 nm pore diameter; and c) 300, 600, and 1000 nm pore diameter.

features. Such structural degradation occurs when the medium surpasses the theoretical porosity limit (∼96%) for IOs [23]. Based on the developed correlation in Equation 2.2, the observable IOs presented in Figure 2.9 increase their porosity from ∼70% to 92% with increasing annealing temperature, while remaining sufficiently below the theoretical limit [24, 26, 59].

2.3.3 Gradient Stacking Order

Through repeated vertical deposition processes and copper electrodeposition, gradient IOs can be obtained. The number of opal layer and pore size are selected by changing the suspension concentration and templated sphere diameter, respectively, as shown in Chapter 2.3.1. Although various combinations of sphere sizes can be stacked on top of each other (see Figure 2.10), there are certain combinations that are not possible due to largely differing sphere diameter ratio.

The sphere size difference as well as the ordering of the stacking strongly affects the quality of the sphere packing at the interfaces between the discrete layers. For instance, results show that larger polystyrene spheres can crystallize on a layer of smaller ones just like on a flat

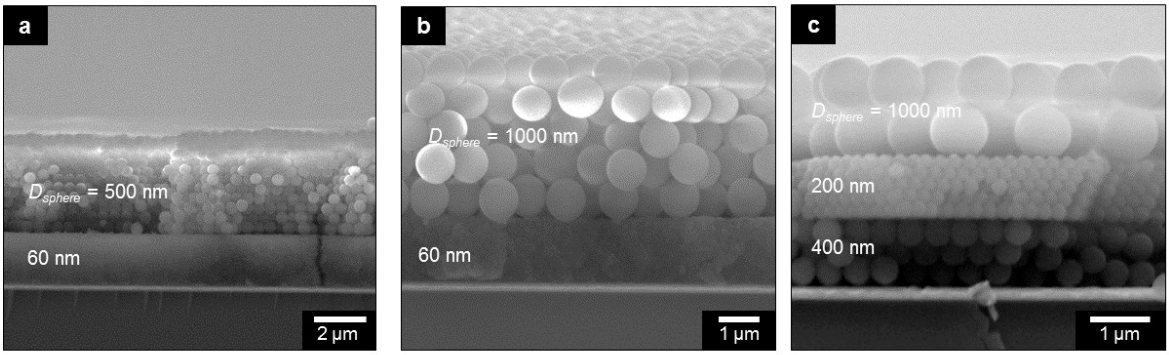

Figure 2.11: Larger spheres can self-assemble onto arrays of smaller spheres to form a discrete interface similar to that on a flat surface. a-c) Cross-sectional SEM showing representative combinations of possible opal stacking.

surface, even with up to about 15 times difference in sizes, i.e., 1000 nm diameter spheres on top of 60 nm diameter spheres (see Figure 2.11). However, having smaller spheres layered on top of larger ones can disturb the crystalline packing, especially when size difference is significant. Instead of forming a discrete flat interface between the layers, the smaller spheres assemble along the curvature of the larger spheres and can often fall into the cavities between the bigger coalesce spheres, as evident in Figure 2.12 where the sphere diameters are 5 times different. From numerous trials, it is concluded that in order for the smaller spheres to consistently crystallize on top of larger spheres like on a flat surface, the colloidal diameter ratio should be less than half, which agrees well with previously fabricated gradient opal structures [42, 43, 44, 47].

2.3.4 Structural Defects

The self-assembly of sacrificial spheres often form crystalline packing arrangements at small length scale (10 μm). However, propagated cracks develop between crystalline domains at larger length scale, creating semi-order template with polycrystalline characteristics (see Figure 1.4a) [26]. The formation of cracks is caused by sphere shrinkage during the drying stage of the newly formed opal [61, 26]. As the colloidal particles shrink in a tightly packed

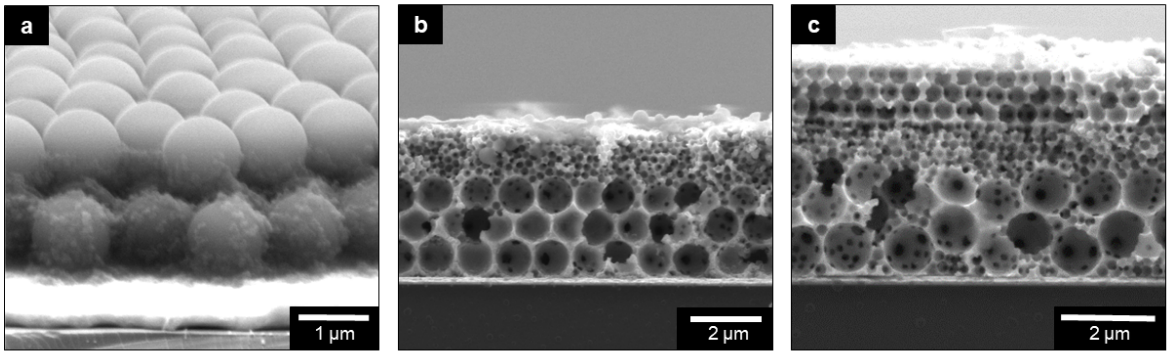

Figure 2.12: The quality of opal film stacking is affected by the sphere diameter ratio and stacking order. Smaller spheres fall through the cavities between larger spheres, as shown with SEM in the a) opal and b) inverse opal state. However, layering larger spheres on top of smaller sphere produces as an undisrupted interfaces, as demonstrated with the subsequent stacking in c).

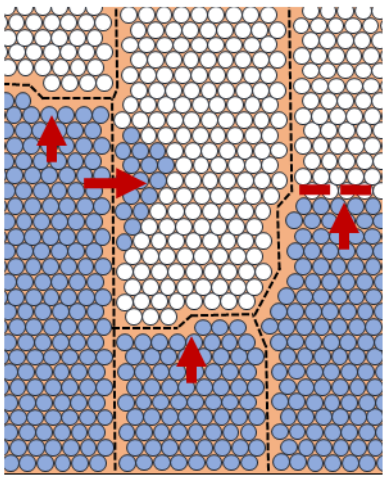

Figure 2.13: Illustration of wall-like grain boundaries between inverse opal domains. Such grain boundaries provide hydraulic resistance to fluid flow and can often halt the flow pathway. Fluid flow can sometimes traverse around the micro-obstruction defects.

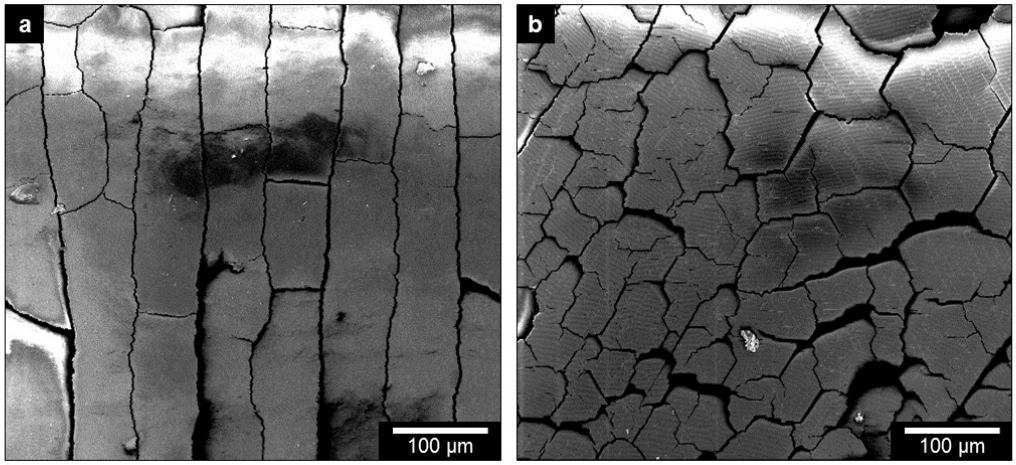

Figure 2.14: Grain domain shapes vary, depending on sphere diameters and self-assembling conditions. Plan view SEM images show typical grain shapes include a) elongated rectangles along the drying direction (using 1000 nm sphere diameter) and b) anisotropic domains (using 300 nm sphere diameter)

array, cracks begin to propagate to alleviate the generated tensile stress [62]. This coalescing event during the opal drying process is further intensified with sample annealing.

The inversion of these cracks during electrodeposition creates impermeable solid walls (see Figure 1.4b), causing significant hydraulic resistance in fluid transport and deviations from predicted transport phenomena within crystalline porous media, as illustrated in Figure 2.13. The characteristic shape of these cracks can often be described as anisotropic or rectangular (see Figure 2.14), depending on the self-assembly process, sphere diameters, and drying direction [63]. Thorough characterization of such crystalline defects and their formations will provide fundamental insights toward the hydraulic transport physics in polycrystalline porous media.

Cross-sectional SEM reveals that the self-assembled opal possesses initial crack widths of approximately 1 - 4 μm depending on the sphere diameters. Annealing the colloidal crystal shows slight increase in crack widths (see Figure 2.15 for results) due to further shrinkage of the spheres and additional coalescent at the sphere-to-sphere contact points. After metal

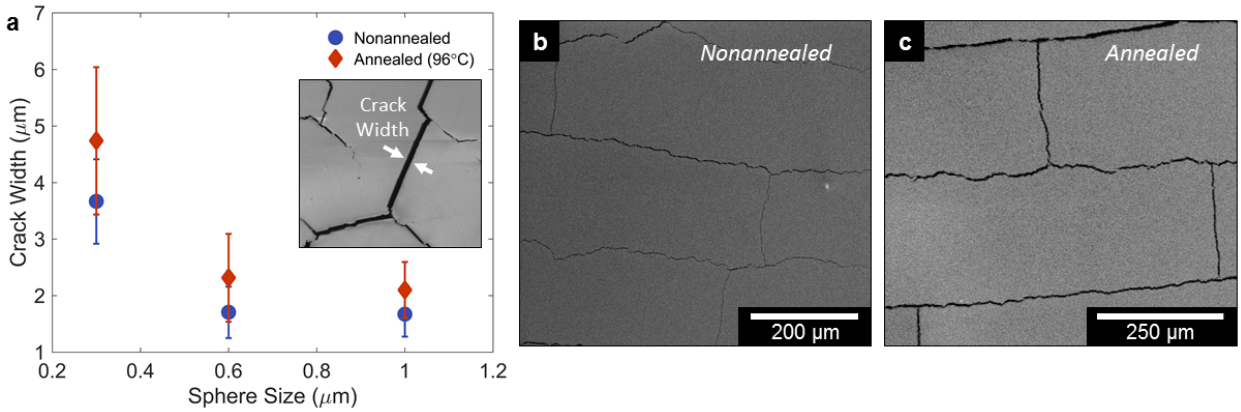

Figure 2.15: The effect of annealing on crack width. a) Annealing condition at 96 °C for 5 hr is performed on opal films with sphere diameters between 300 and 1000 nm. SEM images is used to measure the crack width between the nonannealed and annealed samples. Representative SEM plan view images of b) nonannealed and a) annealed opal film for 1000 nm sphere diameter.

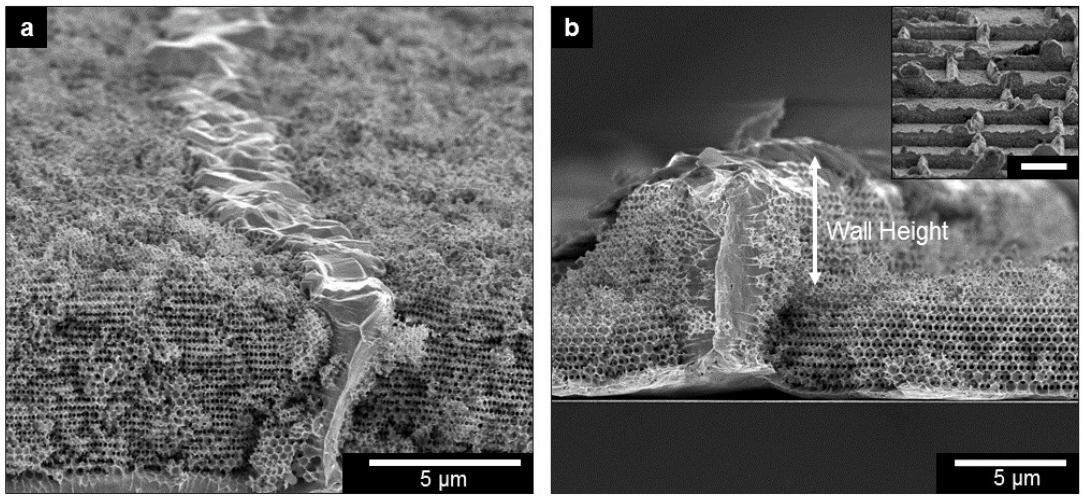

Figure 2.16: The variation in grain boundary wall height is affected by the copper electrodeposition conditions and can be characterized by a) low and b) tall wall height above the domains. The inset provides a top-angled overview of the raised boundaries, with scale bar of 2 μm.

electrodeposition, the heights of the walls are typically ∼1 μm above the IO domains. These raised boundary walls can often stop or slow liquid delivery from continuing across the boundaries, depending on boundary heights. Should the grain boundaries be sufficiently low (i.e., below 1 μm, see Figure 2.16a), wicked fluid may easily overcome the obstructions and occasionally move laterally to neighboring domains, often assisting the continuation of liquid delivery that is trapped by a transverse grain boundary, as illustrated in Figure 2.13). It is also noticed that excessively high current (i.e., $>$ 5.0 mA) in galvanostatic electrodeposition, the boundary height can grow beyond 5 μm above the IO domains and look similar to walls of enclosed cubicles (see Figure 2.16b for example). The towering of the grain boundaries is contributed to the run-away growth of the metal which nucleate the fastest in high electrochemical surface area, i.e., crack regions that are openly exposed to the conductive seed layer. Copper growth within the colloidal crystal remains much slower due to the tortuous pathways between closely-packed spheres. The boundary overgrowth causes the transport to be significantly deterred by such prominent defects. That is, no liquid transport is observed in IOs with tall grain boundary walls.

In addition, the propagation of cracks often disrupts the sphere packings near their dislocation regions, leading to poorer arrangement of pores in its inverted form. The via diameters closest to the grain boundary are often shown to be small or sometimes nonexistence due to the lack of pore interconnectivity. The grain boundaries not only present an impedance of fluid flow over them, but the regions surrounding the boundaries also possess lower fluid permeability, contributing to the edge effect of slowing and even halting the flow of liquid. With smaller pore diameter samples having preferentially smaller grain domain sizes (see Figure 2.17 for statistical distribution of grain sizes with varying pore diameter samples), it suggests that the capillary performance of smaller pore diameters is more dominated by such edge effects.

In order to examine the role of such defects and their associated hydraulic resistances on fluid

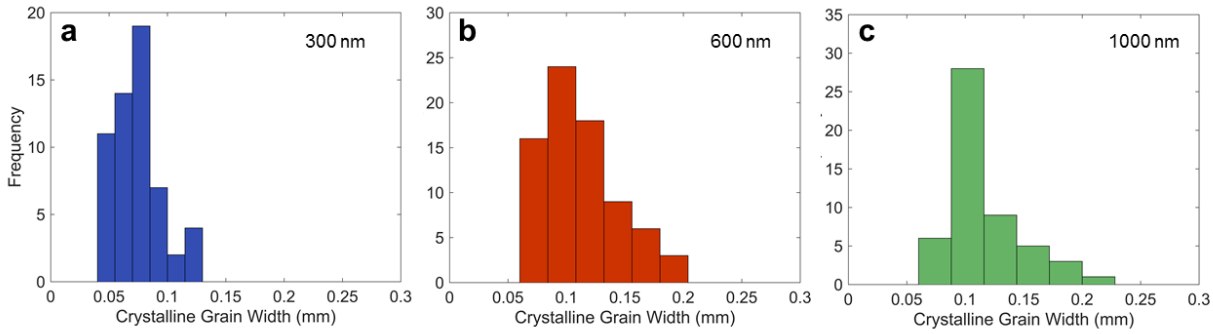

Figure 2.17: Statistical distribution of crystalline grain width with pore diameters of a) 300, b) 600, and c) 1000 nm.

transport through well-ordered porous media, the capillary performances of single crystal domains are compared to those of polycrystalline copper IOs, which are governed by collective IO domains separated by distinct grain boundaries. Elaboration of the results can be found in Chapter 3.2.

2.4 Computational Modeling of Liquid Transport

Analytical modeling is used to examine the trade-off between the capillary force, permeability, and viscous resistance as with varying pore diameters. Wicking dynamics is governed by capillary force which scales inversely with pore diameter and viscous resistance which scales inversely with the square of pore diameter [64]. The capillary force can be described as the hydrostatic-driven pressure in liquid transport, which can be calculated using Young-Laplace capillary equation $4\omega\cos\theta/D_{pore}$, where ω is the surface tension, θ is the static contact angle in surface wettability, and D_{pore} is pore diameter. Utilizing Darcy′s Law, the viscous pressure is dependent upon the wicking material parameters while the flow rate is a function of evaporation mass flux of the system. With constant wicking material parameters, the developed relationship between viscous resistance (red dashed line) and capillary force (solid orange line) with varying pore diameter is shown in Figure 2.20. The balance between

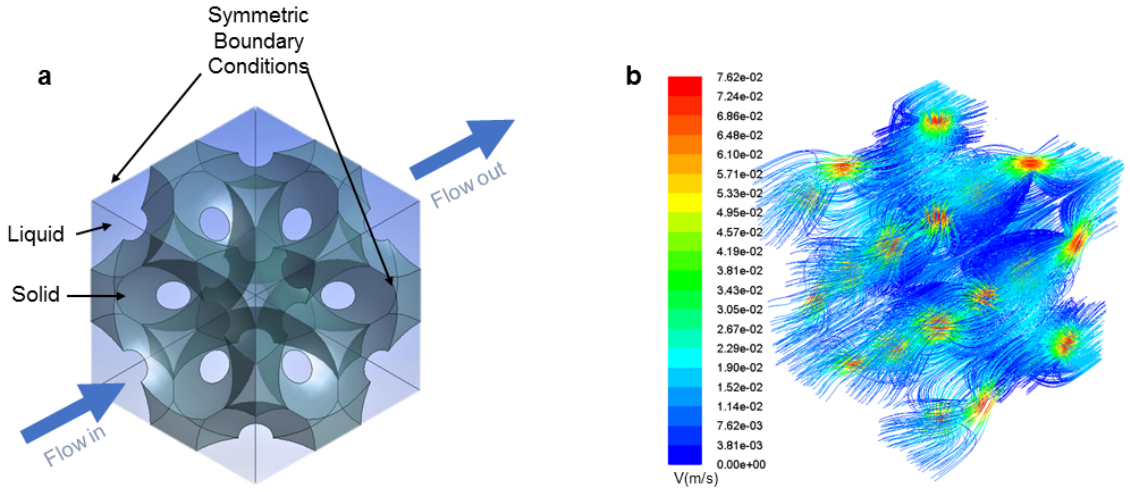

Figure 2.18: Permeability calculation and simulation based on fluid transport through an inverse opal. a) Unit cell of inverse opal with geometry and boundary conditions. The fluid is introduced using 0.01 m/s velocity inlet (left face) and pressure outlet boundary conditions (right face). The other surfaces are set to have symmetric boundary conditions. The gray is the solid domain and blue is the liquid domain. b) A representative modelling of the fluid velocity streamlines inside an inverse opal structure.

these two forces results in a net capillary performance known as the permeability K. Using computational fluid dynamics (CFD) simulation models in ANSYS Fluent (Version 17.1), the permeability values of a unit cell within a IO is separately computed for additional corroboration (Figure 2.18). The calculation of permeability K is obtained using Darcy′s Law [65]:

$$Q = \frac{KA}{\mu(\Delta P/L)} \tag{2.3}$$

Where Q is the volumetric flow rate, A is the cross-section area of the medium, μ is the viscosity of the fluid, and ΔP is the hydrostatic pressure drop, and L is the length of the sample in the flow direction. The unit cell of an IO is represented by an inverted face centered

cubic (FCC) in ANSYS Fluent with assumed overlapped length between pores ranging from 2% to 10% of the pore diameter. The variations in pore overlap results in modulation of via diameters D_{via} range from $D_{via} = 0.2D_{pore}$ with 78% porosity to $D_{via} = 0.4D_{pore}$ with 92% porosity (Figure 2.19).

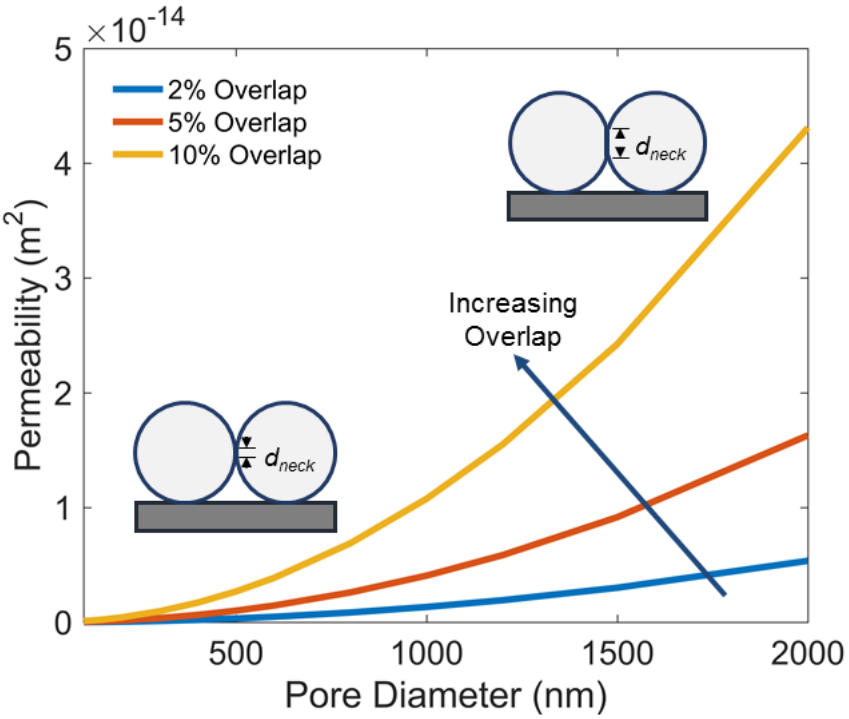

Figure 2.19: The theoretical prediction of permeability in inverse opal structure with varying templated sphere overlap. By increasing the sphere overlap (i.e., increasing the neck diameter), the interconnected window diameter (i.e., via) in inverse opals also increase as a result to enhance in structural permeability.

The CFD simulation model is developed using a single-phase pressure-based solver assuming a steady and laminar flow. Constant velocity is introduced perpendicular to the unit cell inlet (left face) and pressure outlet condition is determined by the right face (see Figure 2.18 for indication of boundary conditions). The other surrounding faces possess symmetric boundary conditions to represent the periodic nature of the unit cell in the IO. Using SIMPLE scheme for pressure-velocity coupling, the pressure gradient ΔP across the unit cell is determined and is plugged into the Darcy's Law equation (Equation 2.4) to determine the permeability

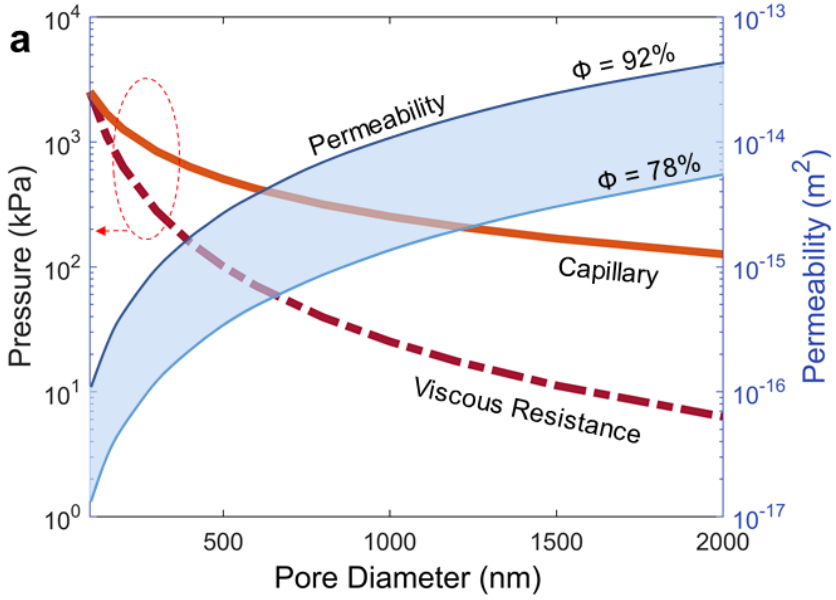

Figure 2.20: Fluid transport physics in single crystals and polycrystalline inverse opals governed by pore morphologies. (a) Fluid transport parameters of capillary forces (solid orange line), viscous resistance (dashed red line), and permeability range (filled blue band) for varying pore diameter D_{pore} and porosity ϕ. The red dashed circle indicates that the capillary and viscous resistance values can be interpreted with the pressure drop on the left y-axis.

K of the unit cell. The derived CFD results is then used to modify the semi-empirical Kozeny-Carman model [66] to relate permeability to porosity. The established correlation [67] of $K = CD_{pore}^2\phi^n$ is modified to $K = D_{pore}^2(0.07\phi^2 - 0.0539\phi)$ for IO structures with porosity ϕ between 78% and 92%. The minimum and maximum ϕ accounts for potential nonuniform annealing of opal film to determine the lower and upper limit of permeability, respectively, as indicated by the blue band in Figure 2.20 for 300 nm $< D_{pore} <$ 2000 nm. The empirically measured permeability of crystalline copper IOs shows good agreement with the computed values as shown in Chapter 3.2.1. High mesh number is used in the simulation model to minimize mesh size effects. For instance, the mesh number used in calculating for a unit cell of $D_{pore} = 1.2$ μm is 393,320.

Chapter 3

Characterization

3.1 Surface Wettability

Wettability describes the surface tension and spreading of a liquid on a material, which is determined by the surface roughness and chemistry [68, 69, 70, 71]. The surface energy can be quantified by wetting the surface with a liquid droplet and examining the droplet contact angle. The surface wettability of a porous media inherently influences the wicking performance of the nanoscale structure. That is, a hydrophobic surface prevents the imbibition of fluid while a hydrophilic surface promotes wicking.

The surface wettability of copper IOs is assessed using sessile drop contact angle method [72]. A pneumatic dispensing system (Kyowa Interface Science) discharges droplet with volumes of ∼10 nL on top of the copper IOs, which have pore diameters in the ranges of nanometers. A high-speed camera (FASTCAM SA8, Photron) captures the discharge at 100,000 fps, and an embedded software (FAMAS) processes and tabulates the evolution of the droplet contact angle using half-angle method. Approximately 10 measurements are obtained for IOs of varying pore diameters. As seen in Figure 3.1, the initial static contact

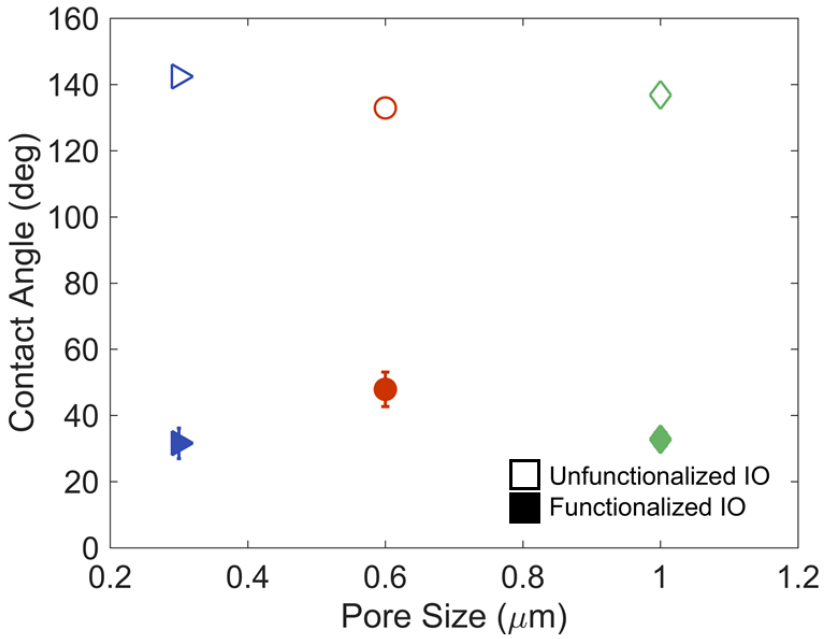

Figure 3.1: The surface wettability of copper inverse opals with varying pore diameters. The as-prepared inverse opals exhibit hydrophobic surfaces (unfilled markers). Through surface functionalization in an aqueous solution of sodium 3-mercapto-1-propanesulfonate, the porous copper media become hydrophilic (filled markers).

angle measurements of DI water on the copper IOs reveal a hydrophobic surface (∼140°), making the microporous copper structure incapable of wicking. In order to lower the surface energy of the copper IOs, the porous media is functionalized in 1 mM of aqueous sodium 3-mercapto-1-propanesulfonate (3-MPS) for at least 24 hours which forms a self-assembly monolayer (SAM) on the surface. After rinsing the functionalized copper IOs in DI water, the contact angle is then remeasured to reveal a hydrophilic surface (∼30 - 50°) that is ideal for microfluidic transport and assessing capillary wicking performance. Thus, all the copper IOs that undergo capillary wicking measurements in this study are functionalized to possess hydrophilic surfaces.

3.2 Capillary Performance of Monoporous Inverse Opals

In evaluating the wicking capability of a porous medium, the key figure of merit is based on the capillary performance parameter, which is defined as the ratio of permeability to effective capillary pore radius K/R_{eff}, where R_{eff}=$0.5D_{pore}cos^{-1}\theta$ and θ is the static contact angle. The capillary performance K/R_{eff} can be experimentally quantified through liquid rate-of-rise measurements [73] (see Figure 3.2). When considering the balance of capillary forces and viscous resistance while neglecting the effect of gravity, Washburn dynamics [74] can be expressed as:

$$h^2 = \frac{4\sigma}{\phi\mu}\frac{K}{R_{eff}}t \tag{3.1}$$

where h is the liquid propagated height, t is the corresponding time, μ is the liquid viscosity, and ϕ is the structural porosity.

As shown in Figure 3.2, a copper IO sample is vertically lowered into a reservoir of DI water using a motorized z-stage. The reservoir remains vapor saturated to minimize the effects of evaporation by enclosing the container with a parafilm that has a thin slit to let the sample through. Once the IO touches the liquid surface, a meniscus from the reservoir quickly latches onto the sample surface. During which, the lowering of the z-stage stops, and the time for wicking experiment starts (i.e., t = 0 sec). A camera captures the rate of liquid propagation up the IO at 120 fps. Post-image processing measure h from the top of the meniscus to the top edge of the liquid front. The width of the IO sample is predefined to be 5 mm by the conductive gold pattern on the substrate, and the thicknesses of the IO film between samples are confirmed to be approximately 10 μm with SEM imaging to ensure

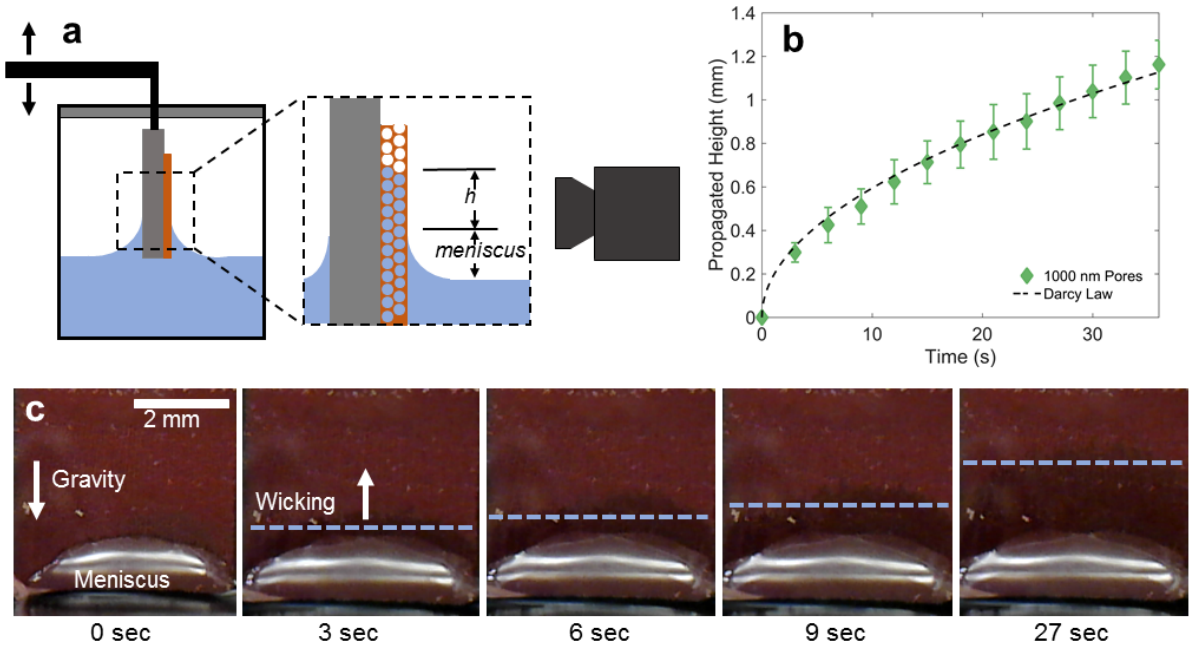

Figure 3.2: Visualization of capillary wicking measurements. a) A schematic for the experimental set-up of capillary wicking. The propagated liquid rises as a function of time which is captured with a camera and then plotted. b) A representative plot of a typical measured wicking height h from a copper inverse opal with a pore diameter of 1000 nm. The dashed line is the numerical trend estimated using Darcy's Law. c) Time evolution images of a copper inverse opal wicking up deionized water. The blue line is a guide for the effective wicking height h_{eff} starting from the average of the meniscus's top edge.

accurate wicking performance comparison.

In monoporous polycrystalline IOs with varying pore diameter from 300 to 1000 nm (Figure 3.3), the capillary performance parameter is estimated by averaging about 40 measurements of h over the width of the sample, yielding an effective capillary rise height h_{eff} as indicated in Figure 3.4. The effective capillary performance parameter for polycrystalline IO K_{eff}/R_{eff} ranges from $\sim 10^{-5}$ to 10^{-3} μm, where K_{eff} is the effective permeability. The resulting K_{eff}/R_{eff} values for polycrystalline IOs are much lower than computationally predicted with CFD models and finite element method (FEM) [24]. Such deviation from theoretical values can be contributed to the grain boundary defects present in the permeable pathway. The grain boundaries cause additional hydraulic resistance that may temporary impede liquid delivery. While the capillary pressure of the adjacent neighboring domains can

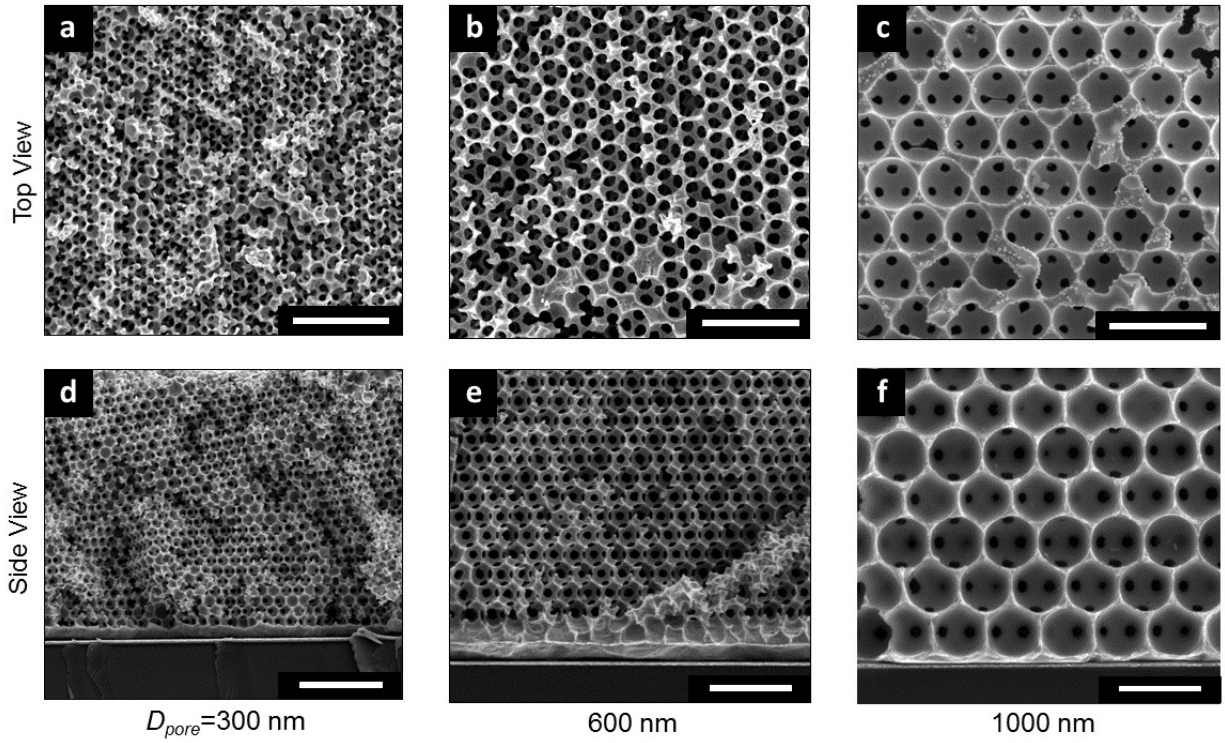

Figure 3.3: A representative set of copper inverse opals with pore diameters of 300, 600, and 1000 nm as shown from a-c) top and d-e) side view SEM images. Scale bars are 2 μm.

assist the trapped fluid with overcoming the physical boundaries, the capillary movement in polycrystalline IOs is characterized with location-dependent fluctuations of continual and lagged liquid flow. Thus, the transport physics in crystalline porous media in the absence of grain boundaries beckons further examination to quantify the hydraulic resistance associated with grain boundaries.

The transport physics in crystalline porous media without the presence of grain boundaries establishes a physical upper bound of transport capability for a given morphology, and such phenomenon can be estimated by examining the liquid rise in individual crystalline domain. Each crystalline grain is mapped as ij, such that subscript i and j represents the rows and columns where the grain is located, respectively. Once the liquid rise is observed in the individual grain, its propagating height h_{ij} is followed until the full length of the grain has been reached with time t_{ij} (see Figure 3.4). The capillary performance parameter of these

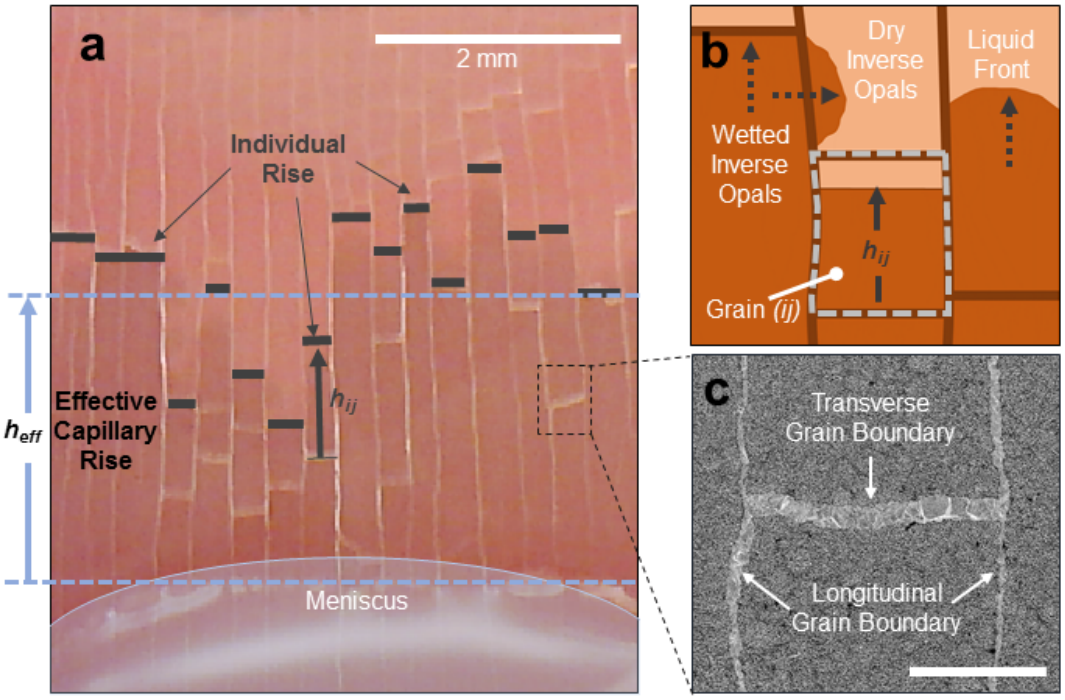

Figure 3.4: Visualization and illustration of microfluidic transport in polycrystalline inverse opals showing individual grain domains and grain boundaries. a) a still photo capture of a vertically placed copper inverse opal wicking up liquid from a reservoir. Due to grain boundary defects, propagated height through each grain column varies across the width of the sample. The average of the general propagated height is determined as the effective capillary rise h_{eff}. b) The illustration of individual grain domains and grain boundaries. The capillary rise h_{ij} within individual grain ij can also be obtained as a function of time t_{ij}. c) Microscopic image showing individual crystalline domains separated by a set of transverse and longitudinal grain boundaries. The scale bar is 100 μm.

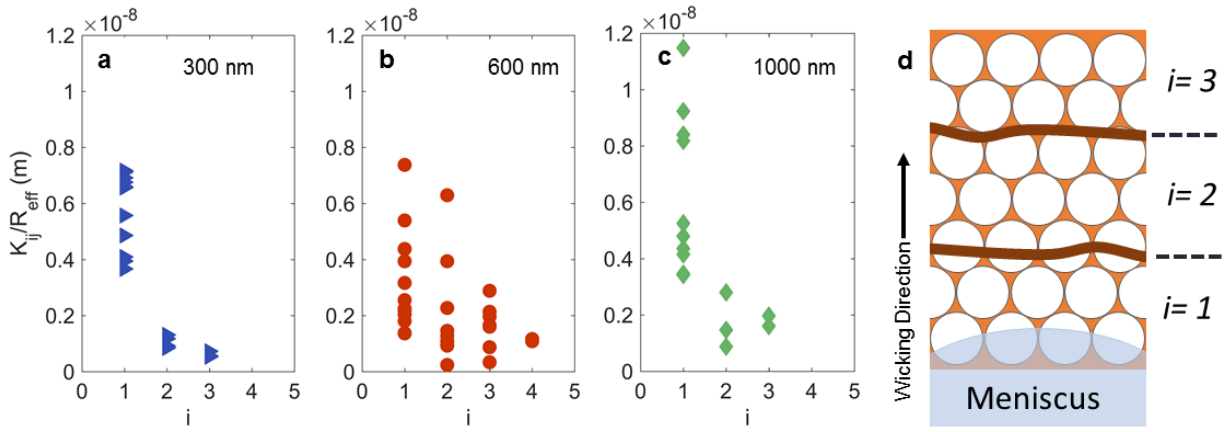

Figure 3.5: The capillary performance of single crystalline grain between series of transverse grain boundaries. With each grain boundary the wicked fluid travels over, i.e., $i > 1$, the capillary performance consistently decrease for a) 300, b) 600, and c) 1000 nm pore diameter samples, contributing significant hydraulic resistance to the effective transport mechanics. d) Illustration of transverse grain boundaries as a series of obstruction for wicking fluid.

individual crystalline grains is denoted as K_{ij}/R_{eff}, such that K_{ij} represents the permeability of the single crystal. In order to accurately compare the K_{ij}/R_{eff} values of different pore diameters, only grains of i =1 (i.e., domains that are in contact with the meniscus region) are analyzed. By wicking fluid directly from the reservoir, the grains that are in contact with the meniscus transport liquid in the absence of grain boundaries so that the only hydraulic resistance present is within the grain domains.

As the fluid is pulled across multiple structural defects with increasing wicking height, the overall hydraulic resistance increases with the collective number of defects that must be overcome. Additional transverse boundaries may restrict the wicking flow of the liquid from its supply source and thus, negatively affecting the resulting capillary performance of individual grains of $i > 1$. The compounding hydraulic resistance can be seen when K_{ij}/R_{eff} is measured at $i = 1$, 2, and 3 for varying pore diameter (Figure 3.5). The capillary performance consistently decreases with the increasing number of defect along the liquid wicking direction. Such collective resistances from boundary defects contributes to K_{eff}/R_{eff} in polycrystalline remaining consistently smaller than K_{ij}/R_{eff} for single crystalline grains by

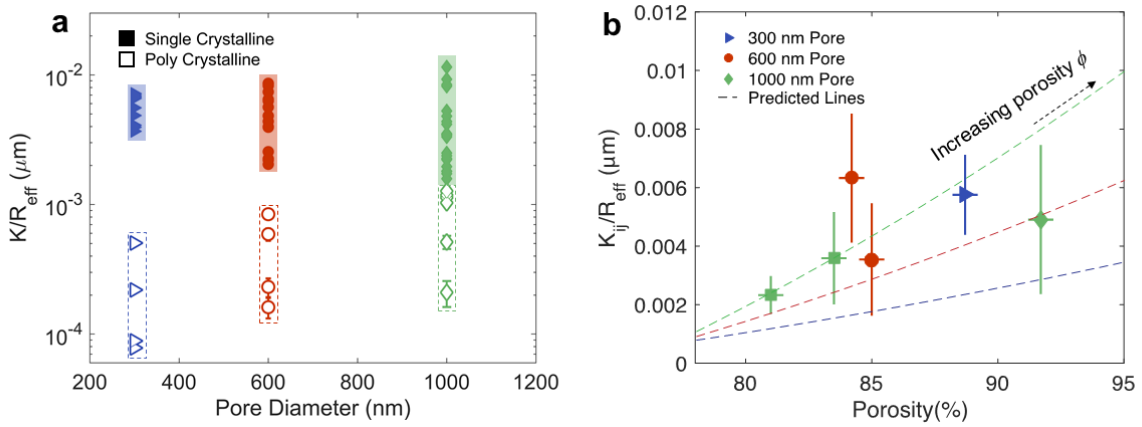

Figure 3.6: The capillary performance parameter K/R_{reff} is the key figure of merit for transport in both single and polycrystalline. a) The capillary performance parameter of the individual crystalline grains of 10^{-3} to 10^{-2} μm (filled markers) is superior to that of polycrystalline samples ranging 10^{-5} to 10^{-3} μm (unfilled markers). b) The individual K_{ij}/R_{reff} of single crystalline grains as a function of porosity ϕ. The dashed lines are predictions from the computational fluid dynamics calculations.

an order of magnitude (Figure 3.6). The experimental measurements of K_{ij}/R_{eff} correspond well with the CFD calculations. For instance, the K_{ij}/R_{eff} of 1000 nm pore diameter ranges from 10^{-3} to 10^{-2} μm, which gives a permeability K range of 10^{-15} to 10^{-14} m^2. The empirical results agree well with the CFD calculated permeability K of 10^{-15} to 10^{-14} m^2 for varying porosity, which can be controlled through annealing conditions.

The capillary performances for both single crystalline and polycrystalline samples increase with increasing pore diameters from 300 nm to 1000 nm, as shown in Figure 3.6a. Despite the general upward trend, large variance in K/R_{eff} exist for both single and polycrystalline IOs with each set of pore diameter. The experimental deviations may be attributed to at least two influencing factors, including 1) porosity variation between the individual grains and 2) porosity variation near the vicinity of grain boundary defects.

The structural porosity ϕ is a critical parameter in determining the overall permeability of the porous matrix. As previously mentioned in Chapter 2.3.2, annealing conditions can be used to roughly modulate the porosity of the IOs, and their associated porosity can be quan-

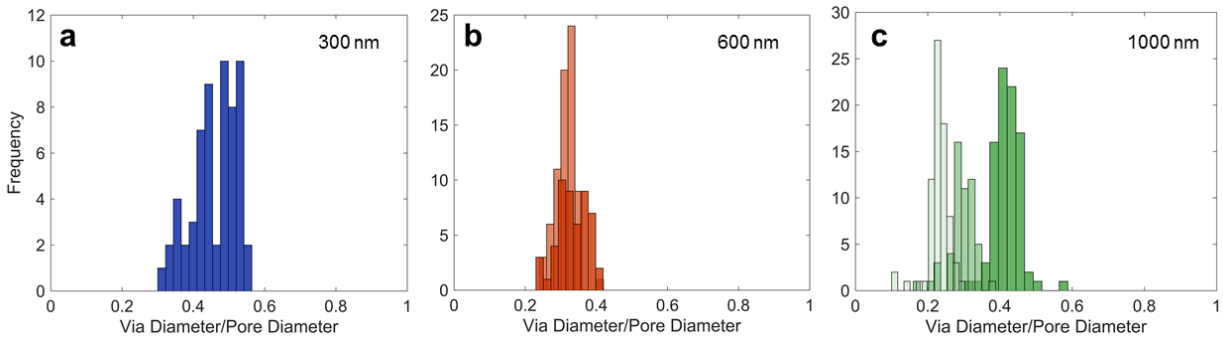

Figure 3.7: Statistical analysis of normalized via diameter D_{via}/D_{pore} for varying pore diameters. The frequency distribution of D_{via}/D_{pore} for a) 300, b) 600, and c) 1000 nm pore diameter samples as indicated by the blue, red, and green bar graph, respectively. The wide range of via diameters for 1000 nm pore diameter samples is attributed to the non-uniform annealing of the samples, which result in three different sets of via diameters that can be seen between three different samples (as indicated by the degree of color transparency).

tified through the normalized via diameter D_{via}/D_{pore} of the structure in Equation 2.2. The established method for IO porosity calculation assumes that sphere sintering occurs isotropically, spheres self-assemble into close-packed crystalline arrangement, and spheres remain perfectly round. However, the accuracy of the derived correlation is expected to deviate when the porosity is significantly greater than typical crystalline-packing of spheres ($\sim$74%). The K_{ij}/R_{eff} for individual crystalline domains of various pore diameters are shown in Figure 3.6b as a function of their corresponding porosities, which demonstrates increasing capillary performance with porosity. The dashed line represents numerical correlation between porosity and K/R_{eff} for various pore diameters. The horizontal error bars are based on the variations of porosity throughout the IO, and such statistical deviations are confirmed in Figure 3.7.

In order to understand the nonuniformity in porosities and large variance in K/R_{eff}, the normalized via diameters are measured at different locations in an IO structure. When observing the via closest to the grain boundary, the D_{via} are often shown to be small or sometimes nonexistent. The lack of pore interconnectivity is caused by sphere-packing disruption from the propagated crack. When the opal film dries after self-assembly, a coalesced

domain of polystyrene spheres would shrink and pack the spheres further inward toward the domain center while the spheres near a crack would be loosely packed. For instance, the D_{via} of 300 nm pore diameter samples are measured near a grain boundary as well as toward the center of the grain domain. The average D_{via} increases by about 10% as the via move away from the grain boundaries, resulting in a 1% increase in the overall porosity. In addition to the wall-like structures creating a physical barrier to hydraulic transport, the regions surrounding the grain boundaries possess lower permeable networks that can slow flow of fluid.

Another source that contributes to the disparity between the experimental and numerical values of porosity and permeability may be caused by the assisted wicking from adjacent grain domains. A wicked liquid can often travel through series of grain domains before stopping its flow at a physical obstruction. Within a certain amount of time, the flow would be able to overcome the barrier. While the hydraulic transport mechanisms across the grain boundary is not fully understood, the apparent interplayed wicking behaviors between bordering domains on the polycrystalline fluid propagation are observed. Such coupling effects in multi-domain systems are difficult to control and cause variation between wicking measurement trials. The microscopic hydraulic interactions in polycrystalline porous media is a phenomenon that presents an investigation of interest for future study.

3.3 Capillary Performance of Gradient Inverse Opals

Monoporous copper IOs reveal fundamental knowledge into the wicking performance in one dimension in the presence of crystalline defects. It is of interest to further investigate the transport physics through three-dimensional heterogeneous porous material. Biological transport systems in nature such as plant veins (see Figure 3.8) utilize heterogeneous porous structure with multiple length scale pores to effectively transport mass and fluid

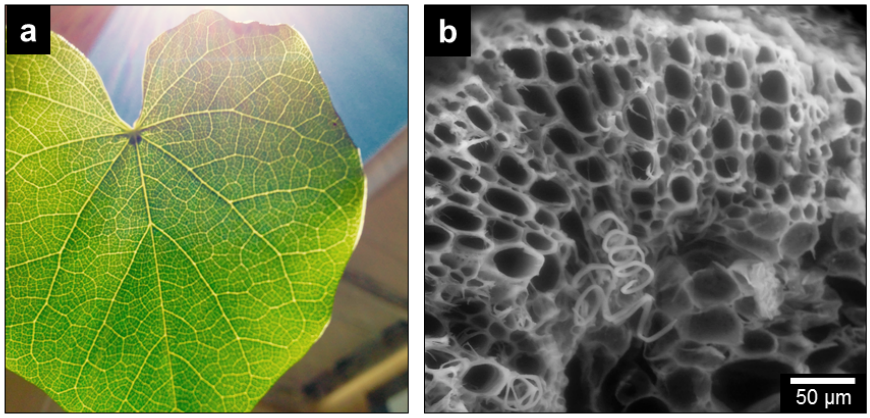

Figure 3.8: Heterogeneous porous materials in biological transport systems and gradient inverse opals. Multilength scales of porous network as seen in (a) plant leaf and (b) stem cross-section (imaged using environmental SEM) are used to emanate novel porous media with heterogeneous structural characteristics.

[50, 75]. To emulate such heterogeneity in crystalline porous media, copper IOs with gradually varying pore sizes is created. Specifically, the gradient IO structure is designed to have stratus composites of individual monoporous layer of 300, 600, and 1000 nm pore diameter with each layer ~7 - 10 μm in thickness.

The effective capillary performance parameter K_{eff}/R_{eff} of such gradient copper IOs is approximately 0.6 - 1.1 x 10^{-3} μm, which is comparable to that of the best single crystal monoporous (i.e., for 1000 nm pore diameter, K_{eff}/R_{eff} = 0.1 - 1.1 x 10^{-3} μm from Figure 3.9) and is also superior to polycrystalline IOs by an order of magnitude. The enhanced wicking performance may be contributed to the multilayering of individual monoporous IOs, which provides alternative and parallel liquid pathways to circumvent a defective region as illustrated in Figure 3.10. The layer-by-layer deposition of pores also suppress these defects to mainly remain within their respective crystal plane and stagger at different regions for parallel pathways to exit.

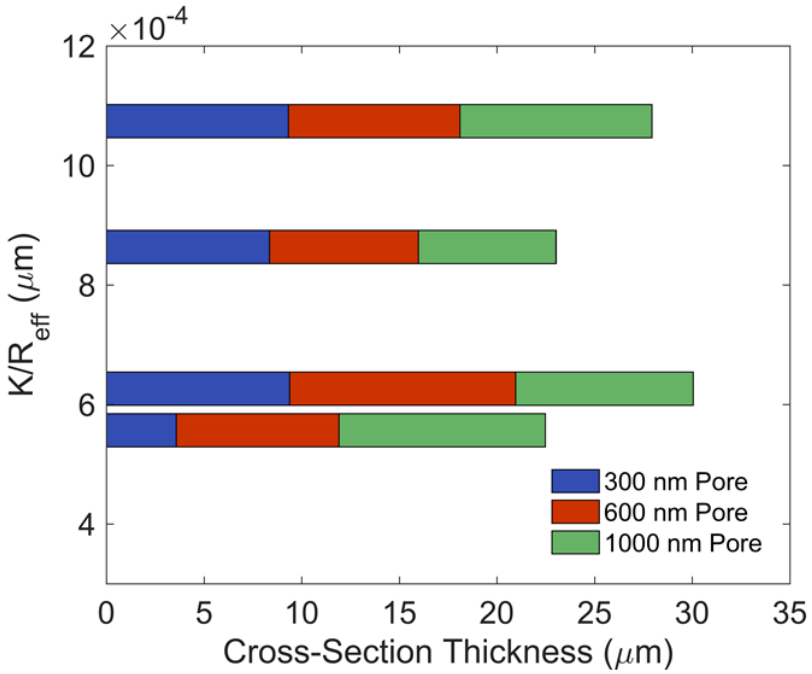

Figure 3.9: The thickness and capillary performance of gradient copper inverse opals. The measured capillary performance of gradient-multilayered copper inverse opals. The stacking arrangement of these gradient IOs have pore diameters of 300, 600, and 1000 nm is examined using SEM to quantify the thickness of individual layers, which are within ∼7 - 10 μm in thickness and are indicated as different colors in the bar graph. The K_{eff}/R_{eff} values of gradient inverse opals are in the range of ∼0.6 - 1.1 x 10^{-3} μm.

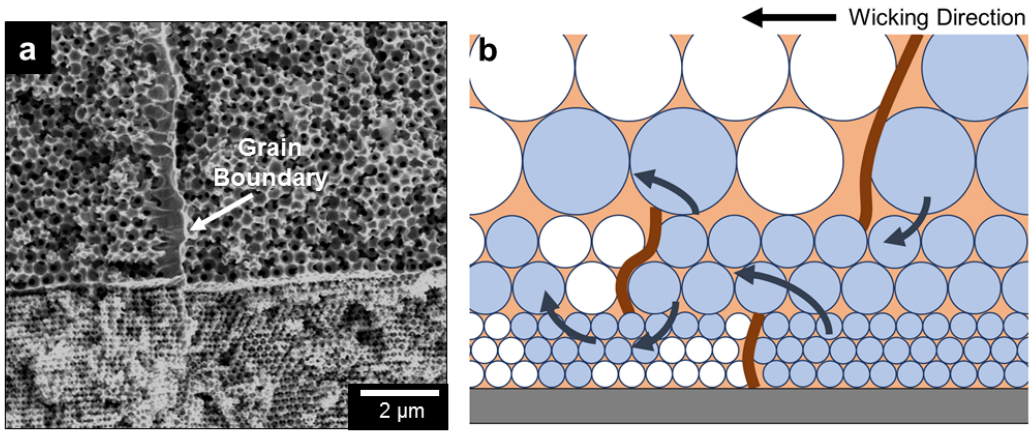

Figure 3.10: Crystalline defects in gradient inverse opals. a) The grain boundaries often remain within their respective crystal plane providing the three-dimensionally spatial staggering of the grain boundaries. (b) The illustration of spatially-varying grain boundaries shows alternative flow pathways in three dimensions, contributing to the enhancement in the effective capillary performance.

3.4 Final Remarks

The enhanced wicking performance of gradient copper IO demonstrates it as a nanoarchitecture with potentials to push beyond the defect-limited transport of polycrystalline porous media for applications in liquid-vapor cooling devices. Since cracks and defects along domain boundaries in opal films and IOs are commonly observed during the self-assembly, drying, and sintering processes, the hydraulic resistance caused by these local defects places an upper limit on the capillary performance of polycrystalline IOs. This study shows that layering multiple films of IOs can further enhance the wicking capability of these porous media by providing alternative flow pathways in three dimensions. In addition to this, the fabrication approach of copper gradient IOs presented in this work offers a new nano- and micro-architecture that provides advantageous wicking capability that can be used for developing the next-generation microfluidic and thermal management devices.

Chapter 4

Conclusion and Future Study

The fabrication of copper IOs is systematically investigated to provide insights toward designing highly-ordered and well-controlled crystalline porous media. During the preparation of IOs, the observed formation of crystalline defects such as cracks create polycrystalline IOs with grain domains and grain boundaries. The capillary performance parameters of both single crystalline and polycrystalline inverse opals are measured with the aim to elucidate the effects of grain boundaries on liquid transport through porous media. Single crystalline copper IOs exhibit an order of magnitude higher capillary performance parameters, independent of the pore diameters, compared to polycrystalline copper IOs whose transport is hindered by the dominant hydraulic resistances of grain boundaries. Inspired by the heterogeneity in biological transport systems, the capillary performance of multilayered IOs having vertically graded pore sizes is studied. These gradient IOs possess capillary performance parameters that are of the same order of magnitude as single crystal grains, which may be attributed to the additional pathways in three dimensions for fluid to circumvent planar defects and thus providing low-resistance parallel hydraulic pathways.

Further work is needed to elucidate the microscopic mechanisms of fluid flow across the

grain boundary defects. When examining the hydraulic transport within each individual grain domain, the laterally neighboring domains would occasionally assist a wicked fluid on overcoming a transverse grain boundary to continue its transport. It is expected that the interplayed wicking behaviors from bordering domains can often affect fluid propagation, which may contribute to the variations in the experimental measurements. In conclusion, the mass transport through engineered porous media is primarily inhibited by morphological defects, including both grain boundaries and low-quality regions near grain boundaries. Improvements in templated porous media for capillary applications will benefit by increasing template quality to reduce defect density.

This work establishes fundamental insights toward understanding, predicting, and engineering hydraulic transport in well-ordered interconnected porous media that can be utilized for microfluidic and two-phase cooling applications. Specifically, the wicking architecture of copper IOs can enhance liquid delivery in planar-type cooling devices as a next-generation thermal management solution.

Bibliography

[1] R. Mahajan, C.-P. Chiu, and G. Chrysler. Cooling a microprocessor chip. *Proceedings of the IEEE*, 94(8):1476–1486, 2006.

[2] U.K. Mishra, L. Shen, T.E. Kazior, and Y.-F. Wu. Gan-based rf power devices and amplifiers. *Proceedings of the IEEE*, 96(2):287–305, 2008.

[3] J.J. Huddle, L.C. Chow, S. Lei, A. Marcos, D.P. Rini, S.J. Lindauer, M. Bass, and P.J. Delfyett. Thermal management of diode laser arrays. In *Semiconductor Thermal Measurement and Management Symposium, 2000. Sixteenth Annual IEEE*, pages 154–160. IEEE, 2000.

[4] M.L. Bauer, Q.N. Pham, C.B. Saltonstall, and P.M. Norris. Thermal conductivity of vertically aligned carbon nanotube arrays: Growth conditions and tube inhomogeneity. *Applied Physics Letters*, 105(15):151909, 2014.

[5] Q.N. Pham, L.S. Larkin, C.C. Lisboa, C.B. Saltonstall, L. Qiu, J.D. Schuler, T.J. Rupert, and P.M Norris. Effect of growth temperature on the synthesis of carbon nanotube arrays and amorphous carbon for thermal applications. *Physica Status Solidi A*, 7:1600852, 2017.

[6] M. Ha and S. Graham. Pool boiling characteristics and critical heat flux mechanisms of microporous surfaces and enhancement through structural modification. *Applied Physics Letters*, 111(9):091601, 2017.

[7] Q. Liao and T.S. Zhao. Evaporative heat transfer in a capillary structure heated by a grooved block. *Journal of Thermophysics and Heat Transfer*, 13(1):126–133, 1999.

[8] C. Li and G.P. Peterson. Evaporation/boiling in thin capillary wicks (ii)effects of volumetric porosity and mesh size. *Journal of Heat Transfer*, 128(12):1320–1328, 2006.

[9] K.C. Leong, C.Y. Liu, and G.Q. Lu. Characterization of sintered copper wicks used in heat pipes. *Journal of Porous Materials*, 4(4):303–308, 1997.

[10] J.A. Weibel, S.V. Garimella, and M.T. North. Characterization of evaporation and boiling from sintered powder wicks fed by capillary action. *International Journal of Heat and Mass Transfer*, 53(19):4204–4215, 2010.

[11] J.A. Weibel, S.S. Kim, T.S. Fisher, and S.V. Garimella. Carbon nanotube coatings for enhanced capillary-fed boiling from porous microstructures. *Nanoscale and Microscale Thermophysical Engineering*, 16(1):1–17, 2012.

[12] Y. Zhu, D.S. Antao, Z. Lu, S. Somasundaram, T. Zhang, and E.N. Wang. Prediction and characterization of dry-out heat flux in micropillar wick structures. *Langmuir*, 32 (7):1920–1927, 2016.

[13] S. Ravi, R. Dharmarajan, and S. Moghaddam. Measurement of capillary radius and contact angle within porous media. *Langmuir*, 31(47):12954–12959, 2015.

[14] M. T. Barako, V. Gambin, and J. Tice. Integrated nanomaterials for extreme thermal management: a perspective for aerospace applications. *Nanotechnology*, 29(15), 2018.

[15] L. Mishchenko, B. Hatton, M. Kolle, and J. Aizenberg. Patterning hierarchy in direct and inverse opal crystals. *Small*, 8(12):1904–1911, 2012.

[16] R. Rengarajan, P. Jiang, D.C. Larrabee, V.L. Colvin, and D.M. Mittleman. Colloidal photonic superlattices. *Physical Review B*, 64(20):205103, 2001.

[17] D. YoubáKim, D. WookáKim, S. HyukáIm, and O. OkáPark. An electrochemically grown three-dimensional porous si@ ni inverse opal structure for high-performance li ion battery anodes. *Journal of Materials Chemistry A*, 2(18):6396–6401, 2014.

[18] M.T. Barako, A. Sood, C. Zhang, J. Wang, T. Kodama, M. Asheghi, X. Zheng, P.V. Braun, and K.E. Goodson. Quasi-ballistic electronic thermal conduction in metal inverse opals. *Nano Letters*, 16(4):2754–2761, 2016.

[19] D.S. Raimundo, B. Hatton, M. Kolle, and J. Aizenberg. Self-assembled polystyrene micro-spheres applied for photonic crystals and templates fabrication. *Journal of Integrated Circuits and System*, 1(3):39–43, 2006.

[20] N.P. Johnson, D.W. McComb, A. Richel, B.M. Treble, and R.M. De La Rue. Synthesis and optical properties of opal and inverse opal photonic crystals. *Synthetic Metals*, 116 (1):469–473, 2001.

[21] S.I. Cho, W.J. Kwon, S.-J. Choi, P. Kim, S.-A. Park, J. Kim, S.J. Son, R. Xiao, S.-H. Kim, and S.B. Lee. Nanotube-based ultrafast electrochromic display. *Advanced Materials*, 17(2):171–175, 2005.

[22] Y. Wang, K. Takahashi, K.H. Lee, and G.Z. Cao. Nanostructured vanadium oxide electrodes for enhanced lithium-ion intercalation. *Advanced Functional Materials*, 16 (9):1133–1144, 2006.

[23] H. Zhang, X. Yu, and P.V. Braun. Three-dimensional bicontinuous ultrafast-charge and-discharge bulk battery electrodes. *Nature Nanotechnology*, 6(5):277–281, 2011.

[24] T.J. Dusseault, J. Gires, M.T. Barako, Y. Won, D.D. Agonafer, M. Asheghi, J.G. Santiago, and K.E. Goodson. Inverse opals for fluid delivery in electronics cooling systems. In *Thermal and Thermomechanical Phenomena in Electronic Systems (ITherm), 2014 IEEE Intersociety Conference on*, pages 750–755. IEEE, 2014.

[25] H. Lee, T. Maitra, J. Palko, C. Zhang, M.T. Barako, Yoonjin Won, M. Asheghi, and K.E. Goodson. Copper inverse opal surfaces for enhanced boiling heat transfer. In *ASME 2017 International Technical Conference and Exhibition on Packaging and Integration of Electronic and Photonic Microsystems*, pages V001T01A006–V001T01A006. American Society of Mechanical Engineers, 2017.

[26] B. Hatton, L. Mishchenko, S. Davis, K.H. Sandhage, and J. Aizenberg. Assembly of large-area, highly ordered, crack-free inverse opal films. *Proceedings of the National Academy of Sciences*, 107(23):10354–10359, 2010.

[27] E. Armstrong, D. McNulty, H. Geaney, and C. ODwyer. Electrodeposited structurally stable v_2o_5 inverse opal networks as high performance thin film lithium batteries. *ACS Applied Materials & Interfaces*, 7(48):27006–27015, 2015.

[28] S. Lee, Y. Lee, D.H. Kim, and J.H. Moon. Carbon-deposited tio_2 3d inverse opal photocatalysts: visible-light photocatalytic activity and enhanced activity in a viscous solution. *ACS Applied Materials & Interfaces*, 5(23):12526–12532, 2013.

[29] J. Li and N. Wu. Semiconductor-based photocatalysts and photoelectrochemical cells for solar fuel generation: A review. *Catalysis Science & Technology*, 5(3):1360–1384, 2015.

[30] R. Malini, U. Uma, T. Sheela, M. Ganesan, and N.G. Renganathan. Conversion reactions: A new pathway to realise energy in lithium-ion battery. *Ionics*, 15(3):301–307, 2009.

[31] Y.-J. Lee and P.V. Braun. Tunable inverse opal hydrogel ph sensors. *Advanced Materials*, 15(7-8):563–566, 2003.

[32] R.C. Schroden, M. Al-Daous, C.F. Blanford, and A. Stein. Optical properties of inverse opal photonic crystals. *Chemistry of Materials*, 14(8):3305–3315, 2002.

[33] G. Collins, M. Blomker, M. Osiak, J.D. Holmes, M. Bredol, and C. ODwyer. Three-dimensionally ordered hierarchically porous tin dioxide inverse opals and immobilization of palladium nanoparticles for catalytic applications. *Chemistry of Materials*, 25(21): 4312–4320, 2013.

[34] G. Guan, R. Zapf, G. Kolb, V. Hessel, H. Löwe, J. Ye, and R. Zentel. Preferential co oxidation over catalysts with well-defined inverse opal structure in microchannels. *International Journal of Hydrogen Energy*, 33(2):797–801, 2008.

[35] A. Esmanski and G.A. Ozin. Silicon inverse-opal-based macroporous materials as negative electrodes for lithium ion batteries. *Advanced Functional Materials*, 19(12):1999–2010, 2009.

[36] J. Liu, H.G. Zhang, J. Wang, J. Cho, J.H. Pikul, E.S. Epstein, X. Huang, J. Liu, W.P. King, and P.V. Braun. Hydrothermal fabrication of three-dimensional secondary battery anodes. *Advanced Materials*, 26(41):7096–7101, 2014.

[37] S.-C. Wong, J.-H. Liou, and C.-W. Chang. Evaporation resistance measurement with visualization for sintered copper-powder evaporator in operating flat-plate heat pipes. *International Journal of Heat and Mass Transfer*, 53(19):3792–3798, 2010.

[38] M.A. Hanlon and H.B. Ma. Evaporation heat transfer in sintered porous media. *Transactions-American Society of Mechanical Engineers Journal of Heat Transfer*, 125 (4):644–652, 2003.

[39] M. Annamalai and S. Dhanabal. Experimental studies on porous wick flat plate heat pipe. *International Refrigeration & Air Conditioning Conference*, 2010.

[40] J.-H. Liou, C.-W. Chang, C. Chao, and S.-C. Wong. Visualization and thermal resistance measurement for the sintered mesh-wick evaporator in operating flat-plate heat pipes. *International Journal of Heat and Mass Transfer*, 53(7):1498–1506, 2010.

[41] Y.S. Zhang, K.P. Regan, and Y. Xia. Controlling the pore sizes and related properties of inverse opal scaffolds for tissue engineering applications. *Macromolecular Rapid Communications*, 34(6):485–491, 2013.

[42] Z. Cai, Y.J. Liu, J. Teng, and X. Lu. Fabrication of large domain crack-free colloidal crystal heterostructures with superposition bandgaps using hydrophobic polystyrene spheres. *ACS Applied Materials & Interfaces*, 4(10):5562–5569, 2012.

[43] R. Kubrin, R.M. Pasquarelli, M. Waleczek, H.S. Lee, R. Zierold, J.J. do Rosário, P.N. Dyachenko, J.M. Montero Moreno, A.Y. Petrov, and R. Janssen. Bottom-up fabrication of multilayer stacks of 3d photonic crystals from titanium dioxide. *ACS Applied Materials & Interfaces*, 8(16):10466–10476, 2016.

[44] Q. Yan, L.K. Teh, Q. Shao, C.C. Wong, and Y.-M. Chiang. Layer transfer approach to opaline hetero photonic crystals. *Langmuir*, 24(5):1796–1800, 2008.

[45] H. Huang, J. Chen, Y. Yu, Z. Shi, H. Möhwald, and G. Zhang. Controlled gradient colloidal photonic crystals and their optical properties. *Colloids and Surfaces A: Physicochemical and Engineering Aspects*, 428:9–17, 2013.

[46] P. Jiang, J.F. Bertone, K.S. Hwang, and V.L. Colvin. Single-crystal colloidal multilayers of controlled thickness. *Chemistry of Materials*, 11(8):2132–2140, 1999.

[47] P. Jiang, G.N. Ostojic, R. Narat, D.M. Mittleman, and V.L. Colvin. The fabrication and bandgap engineering of photonic multilayers. *Advanced Materials*, 13(6):389–393, 2001.

[48] G.B. West, J.H. Brown, and B.J. Enquist. A general model for the origin of allometric scaling laws in biology. *Science*, 276(5309):122–126, 1997.

[49] G.B. West, J.H. Brown, and B.J. Enquist. A general model for the structure and allometry of plant vascular systems. *Nature*, 400(6745):664–667, 1999.

[50] T.J. Brodribb, T.S. Feild, and G.J. Jordan. Leaf maximum photosynthetic rate and venation are linked by hydraulics. *Plant Physiology*, 144(4):1890–1898, 2007.

[51] R.G. Shimmin, A.J. DiMauro, and P.V. Braun. Slow vertical deposition of colloidal crystals: A langmuir- blodgett process? *Langmuir*, 22(15):6507–6513, 2006.

[52] A.S. Dimitrov and K. Nagayama. Continuous convective assembling of fine particles into two-dimensional arrays on solid surfaces. *Langmuir*, 12(5):1303–1311, 1996.

[53] M.A. McLachlan, N.P. Johnson, M. Richard, and D.W McComb. Thin film photonic crystals: Synthesis and characterisation. *Journal of Materials Chemistry*, 14(2):144–150, 2004.

[54] Y.-H. Ye, F. LeBlanc, A. Haché, and V.-V. Truong. Self-assembling three-dimensional colloidal photonic crystal structure with high crystalline quality. *Applied Physics Letters*, 78(1):52–54, 2001.

[55] N. Sapoletova, T. Makarevich, K. Napolskii, E. Mishina, A. Eliseev, A. van Etteger, T. Rasing, and G. Tsirlina. Controlled growth of metallic inverse opals by electrodeposition. *Physical Chemistry Chemical Physics*, 12(47):15414–15422, 2010.

[56] A.V. Chumakova, G.A. Valkovskiy, A.A. Mistonov, V.A. Dyadkin, N.A. Grigoryeva, N.A. Sapoletova, K.S. Napolskii, A.A. Eliseev, Andrei V. Petukhov, and S.V. Grigoriev. Periodic order and defects in ni-based inverse opal-like crystals on the mesoscopic and atomic scale. *Physical Review B*, 90(14):144103, 2014.

[57] T. Sumida, Y. Wada, T. Kitamura, and S. Yanagida. Construction of stacked opaline films and electrochemical deposition of ordered macroporous nickel. *Langmuir*, 18(10): 3886–3894, 2002.

[58] L.V. Mikhnev, E.A. Bondarenko, .. Chapura, A.A. Skomorokhov, and A.A. Kravtsov. Influence of annealing temperature on optical properties of the photonic-crystal structures obtained by self-organization of colloidal microspheres of polystyrene and silica. *Optical Materials*, 75:453–458, 2017.

[59] I.-L. Ngo and C. Byon. Permeability of microporous wicks with geometric inverse to sintered particles. *International Journal of Heat and Mass Transfer*, 92:298–302, 2016.

[60] J. Rieger. The glass transition temperature of polystyrene: Results of a round robin test. *Journal of Thermal Analysis and Calorimetry*, 46(3-4):965–972, 1996.

[61] A.A. Chabanov, Y. Jun, and D.J. Norris. Avoiding cracks in self-assembled photonic band-gap crystals. *Applied Physics Letters*, 84(18):3573–3575, 2004.

[62] T. Xia, W. Luo, F. Hu, W. Qiu, Z. Zhang, Y. Lin, and X.Y. Liu. Fabrication of crack-free photonic crystal films on superhydrophobic nanopin surface. *ACS Applied Materials & Interfaces*, 9(26):22037–22041, 2017.

[63] A. Hartsuiker and W.L. Vos. Structural properties of opals grown with vertical controlled drying. *Langmuir*, 24(9):4670–4675, 2008.

[64] F.A.L. Dullien. *Porous media: fluid transport and pore structure*. Academic press, 2012.

[65] H. Darcy. *Les fontaines publiques de la ville de Dijon: exposition et application...* Victor Dalmont, 1856.

[66] P. Xu and B. Yu. Developing a new form of permeability and kozeny–carman constant for homogeneous porous media by means of fractal geometry. *Advances in Water Resources*, 31(1):74–81, 2008.

[67] T. Bourbie, O. Coussy, B. Zinszner, and M.C. Junger. Acoustics of porous media. *The Journal of the Acoustical Society of America*, 91(5):3080–3080, 1992.

[68] Y.H. Yeong, A. Milionis, E. Loth, and I.S. Bayer. Microscopic receding contact line dynamics on pillar and irregular superhydrophobic surfaces. *Scientific Reports*, 5:8384, 2015.

[69] C. Frankiewicz and D. Attinger. Texture and wettability of metallic lotus leaves. *Nanoscale*, 8(7):3982–3990, 2016.

[70] A. Davis, Y.H. Yeong, A. Steele, I.S. Bayer, and E. Loth. Superhydrophobic nanocomposite surface topography and ice adhesion. *ACS Applied Materials & Interfaces*, 6(12): 9272–9279, 2014.

[71] P.P. Dubey, Q.N. Pham, H. Cho, Y. Kim, and Y. Won. Controlled wetting properties through heterogeneous surfaces containing two-level nanofeatures. *ACS Omega*, 2(11): 7916–7922, 2017.

[72] I. Kiper, R. Fulcrand, C. Pirat, G. Simon, B. Stutz, and S.M.M. Ramos. Sessile drop evaporation on (super) hydrophobic surfaces: Effect of low pressure on the contact line dynamics. *Colloids and Surfaces A: Physicochemical and Engineering Aspects*, 482: 617–623, 2015.

[73] Y. Nam, S. Sharratt, C. Byon, S. J. Kim, and Y. S. Ju. Capillary performance of bi-porous sintered metal wicks. *International Journal of Heat and Mass Transfer*, 55: 4096–4103, 2012.

[74] Y. Nam, S. Sharratt, C. Byon, S. J. Kim, and Y. S. Ju. Fabrication and characterization of the capillary performance of superhydrophilic cu micropost arrays. *Jounral of Microelectromechanical System*, 19:581–588, 2010.

[75] T.L. Slewinski, C. Zhang, and R. Turgeon. Structural and functional heterogeneity in phloem loading and transport. *Frontiers in Plant Science*, 4:1–11, 2013.